We are IntechOpen, the world's leading publisher of Open Access books
Built by scientists, for scientists

6,900
Open access books available

185,000
International authors and editors

200M
Downloads

154
Countries delivered to

Our authors are among the

TOP 1%
most cited scientists

12.2%
Contributors from top 500 universities

BOOK CITATION INDEX
CLARIVATE ANALYTICS
INDEXED

WEB OF SCIENCE™

Selection of our books indexed in the Book Citation Index
in Web of Science™ Core Collection (BKCI)

Interested in publishing with us?
Contact book.department@intechopen.com

Numbers displayed above are based on latest data collected.
For more information visit www.intechopen.com

Polymer Nanowires

Baojun Li and Xiaobo Xing

State Key Laboratory of Optoelectronic Materials and Technologies,
School of Physics and Engineering, Sun Yat-Sen University, Guangzhou 510275,
China

1. Introduction

The development of nanotechnology in photonics offers significant scientific and technological potentials [1,2]. It fosters the substantial efforts for exploring novel materials, developing easy fabrication techniques, reducing the size of photonic components, improving device integration density, and fabricating low-cost nanodevices. Since nanometer-scale photonic wires are highly desirable for applications in high density and miniaturized photonic integrated circuits (PICs), subwavelength-diameter wires have been drawn and demonstrated by flame-heated silica fiber [3] and bulk glasses [4] methods. The method provides an easy and cheap photonic wires manufacturing technique, but a steady temperature distribution is required in the drawing region and the lengths of the fabricated wires are limited to 4 mm and tens of millimeters. Later, flame-brushing and microheater-brushing techniques were proposed to fabricate nanowires from silica fibers [5−7] and compound-glass fibers [8], respectively. The length of the fabricated nanowire is extended to 110 mm, but this technique requires extremely good control of processing temperature and airflow around the nanowires. On the other hand, due to relatively low flexibility of silica and glasses, only wire-based simple devices such as 2×2 branch coupler [4,9], single-ring resonantor [3,9], and single Mach-Zehnder (MZ) interferometer [10] were assembled and demonstrated. Compared with silica and glasses, polymers have high flexibility, and thus can be randomly bent/squeezed and molded to have variety of shapes [11,12].

In this chapter, we will introduce a novel polymer material of poly(trimethylene terephthalate) (PTT) which was used for the first time in nanophotonics. Then we will introduce a simple PTT polymer fabrication method, i.e. one-step drawing process. Followed by a description of a series of ultracompact devices and nanophotonic device arrays assembled by the PTT nanowires. Final is a perspective.

2. PTT polymer

PTT polymer can be extracted from petroleum or refined from corn and was original being used in carpet and textile. It was first synthesized by Whinfield and Dickson [13]. It is a semicrystalline aromatic polyester synthesized by the polycondensation of terephthalic acid and 1,3-propanediol (PDO) [14]. Mainly because of its raw materials, PDO, was very expensive, so the PTT with three methylene groups in the polymer's repeating unit remained an obscure polymer and never went beyond laboratory status despite having some

outstanding properties as a textile fiber [15]. Fortunately, recent breakthroughs in PDO synthesis via hydroformylation of ethylene oxide [16], process improvements in the traditional synthetic route through acrolein and the promising bio-engineering route using glycerol as starting material for PDO have reduced the price of PDO by at least an order of magnitude. PTT is made by the melt polycondensation of PDO with either terephthalic acid or dimethyl terephthalate. The chemical structure is shown as follows:
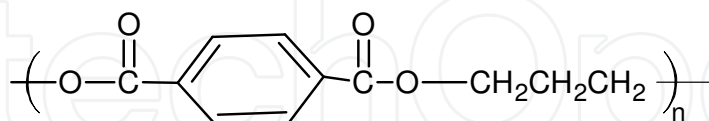
2.1 Thermal properties

PTT is a semicrystalline polymer with a differential scanning calorimetry (DSC) peak melting point of 228 °C. The equilibrium melting points, T_m, are 238 °C [17, 18], 244 °C [19] and 248 °C [20, 21]. Since the T_m values of semicrystalline polymers are usually 15–25 °C higher than their DSC T_m values, and also because the lower-melting poly(butylenes terephthalate) (PBT) has a T_m of 245 °C, it is not unreasonable to assume that 248 °C might be a more appropriate T_m for PTT.

Double DSC melting peaks are frequently observed in PTT, especially when scanning at a low heating rate of < 5 °C/min. Huang *et al.* [21] studied the effect of crystallization temperature, time and cooling rate on these PTT double melting peaks. PTT had two melting peaks at about 222 and 228 °C when it was crystallized at 210 °C between 10 and 60 min. With prolonged crystallization to 360 min, the two peaks merged into one with a peak temperature of 225.5 °C. However, when it was crystallized at a lower temperature of 180 °C, instead of having two melting peaks, PTT had a main 228 °C endotherm with a shoulder at about 219 °C. Unlike the 210 °C crystallized samples, prolonging the crystallization time to 360 min did not change the overall shape of the DSC curves. The lower-melting shoulder persisted and moved slightly to a higher temperature. The origin of the double melting peaks was attributed to the lower-melting crystals being recrystallized and melted at a higher temperature during the heating scan, or to the polymer having two populations of crystals of substantially different sizes.

2.2 Mechanical and physical properties

The mechanical and physical properties of PTT [22], measured from injection molded American Society of Testing Methods (ASTM) Type II samples, is given in Table 1.

2.3 Intrinsic birefringence

Birefringence is the difference between the refractive index parallel, $n_{//}$, and perpendicular, $n_\perp$, to the draw direction. When the polymer is perfectly oriented, the birefringence is called intrinsic birefringence. For PTT crystal, the average refractive index, $n_{av} = (n_{xx} + n_{yy} + n_{zz})/3$, was found 1.638 [24].

For uniaxial orientation, the transverse refractive index $n_\perp$ of PTT, averaged from $(n_{xx} + n_{yy})/2$, was 1.636. The intrinsic birefringence of PTT crystal, $\Delta n_c^o = n_{//} - n_\perp$ was 0.029. The two-phase model explains why highly oriented PTT has such a low birefringence; the contribution of the crystalline-phase orientation to the overall birefringence is very small, although the polymer crystallinity and degree of crystal orientation are very high.

Property	PTT
Tensile strength (MPa)	67.6
Flexural modulus (GPa)	2.76
Heat distortion temperature, at 1.8 MPa (°C)	59
Notched Izod impact (J/m)	48
Specific gravity	1.35
Mold shrinkage (m/m)	0.02
Dielectric strength (V/mil)	530
Dielectric constant, at 1 MHz	3.0
Dissipation factor, at 1 MHz	0.015
Volume resistivity (ohm cm)s	1.00×10^{16}

Table 1. The mechanical and physical properties of PTT [22, 23]

2.4 Transmittance

PTT (M_n =17,300, M_w =35,200, Shell Chemical Company) was compression molded at 250 °C into 25-µm-thick film. It was quenched in water. Wide-angle X-ray diffraction data (WAXD) were taken on a Bruker D8 Advance Diffractometer (Germany). Figure 1 shows the WAXD spectra of PTT film. There is no apparent diffraction peak in the WAXD pattern, so the PTT film is amorphous pattern. Figure 2 shows that the transmittance of the PTT film (25-µm amorphous film) is about 90% in the wavelength region of 400 to 2000 nm [25]. Its good transparency from visible to near-infrared together with its relatively large refractive index (1.638) [24] can provide fine optical confinement for advanced nanowires and nanophotonic devices.

2.5 Elastic recovery

The fiber industry has long been aware of PTT's good tensile elastic recovery. Ward *et al*. [15] studied the deformation behavior of PTT fiber. Figure 3 shows that the PTT elastic recovery and permanent set nearly tracked that of nylon 66 up to 30% strain.
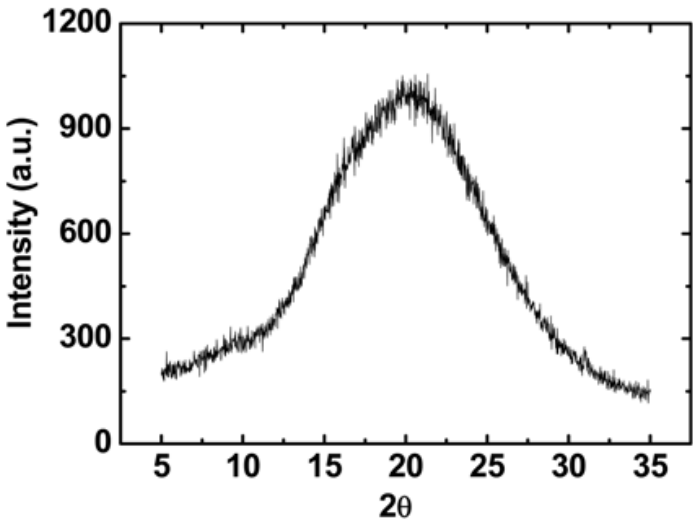
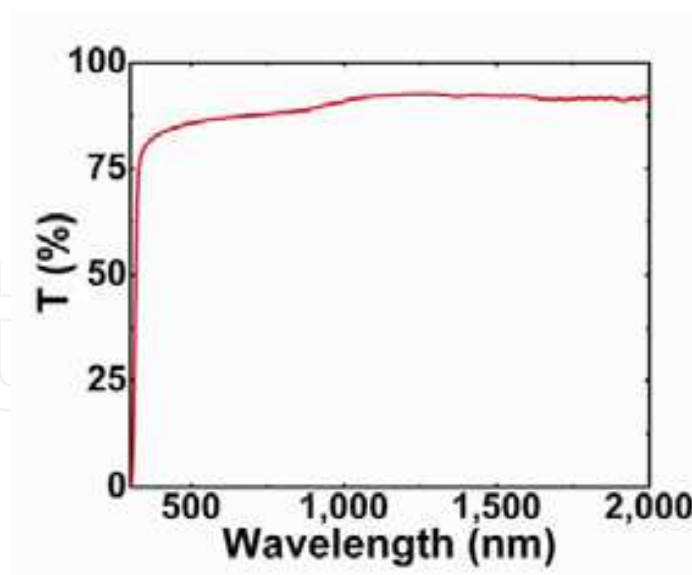

Fig. 1. The WAXD spectra of a 25-µm-thick PTT film.

Fig. 2. Room-temperature transmission spectrum of a 25-µm-thick amorphous PTT film. It shows the transmittance of about 90% in the wavelength region of 400 to 2000 nm.
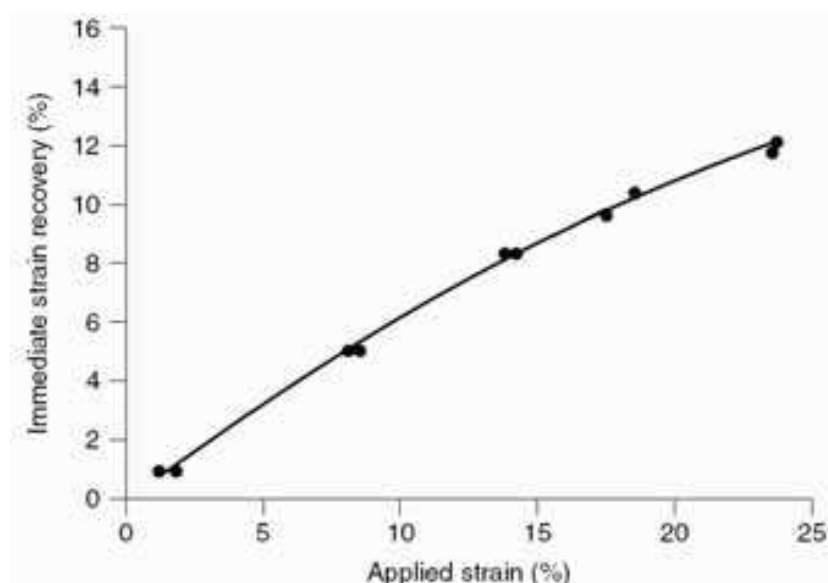

Fig. 3. PTT elastic recovery at various strains [26]

The unusually good PTT elastic recovery property was thought to relate to the plateau region of its stress–strain curve. Jakeways *et al*. [27] deformed PTT fiber *in situ* in a wide-angle X-ray diffractometer, and measured the changes in the fiber period *d*-spacing along the *c*-axis as a function of strain. The crystalline chain responded and deformed immediately to the applied strain. It increased in direct proportion to the applied strain up to 4% before deviating from affine deformation (Figure 4). Furthermore, the deformation below this critical strain was reversible. This microscopic reversible crystal deformation was tied to PTT chain conformation. Since initial deformation involves torsional rotation of the *gauche* methylene C–C bonds, the force is only a fraction of the bond stretching force. Thus, polymer with a helical chain conformation tends to have a low crystal modulus, about 20% of the predicted modulus if the chains were in all-*trans* conformations [28].
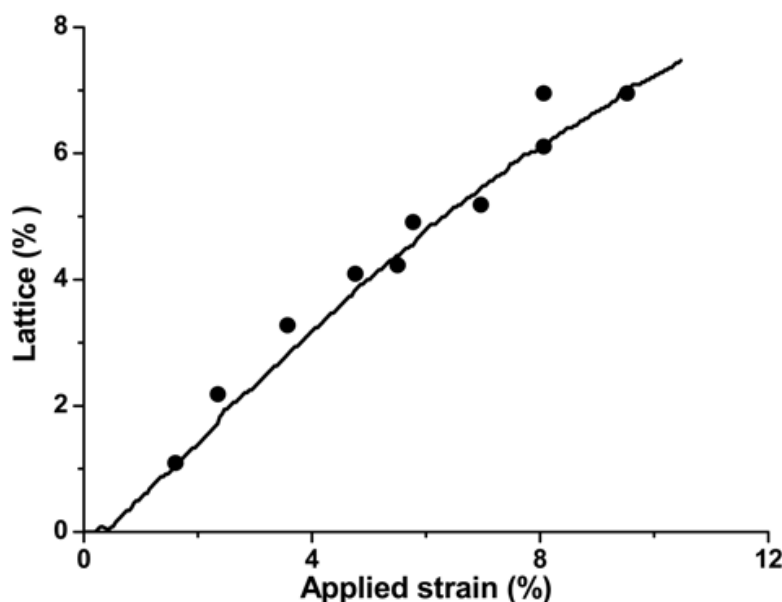
Fig. 4. Changes of PTT fiber *c*-axis lattice strains measured from X-ray diffraction spacings as a function of applied external strains [26].

PTT indeed has a very low X-ray crystal modulus of 2.59 GPa [29]. This value is probably too low because a highly oriented PTT fiber with about 50% crystallinity already had a 2.5 GPa modulus [15]. Using the CERRIUS II molecular simulation program, Jo [30] calculated a 12.2 GPa crystal modulus. Because of the low crystal modulus, the PTT crystalline chain responded and deformed immediately with applied macroscopic strain. The crystalline chain deformation is reversible, and is the driving force for the good elastic recovery. Jakeways *et al*. [27] addressed only the crystalline chain deformation to explain PTT's elastic recovery. The macroscopic deformation must also simultaneously involve the partially irreversible amorphous chain deformation. The higher the applied strain, then the more dominant was the irreversible amorphous deformation with deviation from affine deformation.

2.6 Drawing behavior

Figure 5 shows the tensile stress–strain curves of PTT at various temperatures [31]. At room temperature, PTT is ductile. It yields at 5.4% strain, cold draws with a natural draw ratio of about 3.2, strain-hardens and breaks at 360% strain. With increasing draw temperature, the yield stress decreases and the elongation at break increases. At 50 °C, just above the glass transition temperature, T_g, PTT becomes rubbery. The Young's modulus decreases by about two orders of magnitude from 1140 to 12.9 MPa, and the overall drawability increases with a strain at break of nearly 600%. However, when the draw temperature was increased to 75 °C, 30 °C above the T_g, instead of becoming more rubbery and capable of higher draw, PTT became ductile again. The modulus unexpectedly increased by more than tenfold to 189 MPa. The overall drawability decreased with a drop in breaking strain to 390%. In fact, the 75 °C stress–strain curve looked similar to that of the one room temperature. Instead of the conventional experience of increasing drawability with increasing temperature, the PTT draw first increased, went through a maximum and decreased, all happening over a narrow range of temperature from room temperature to T_g +30 °C.
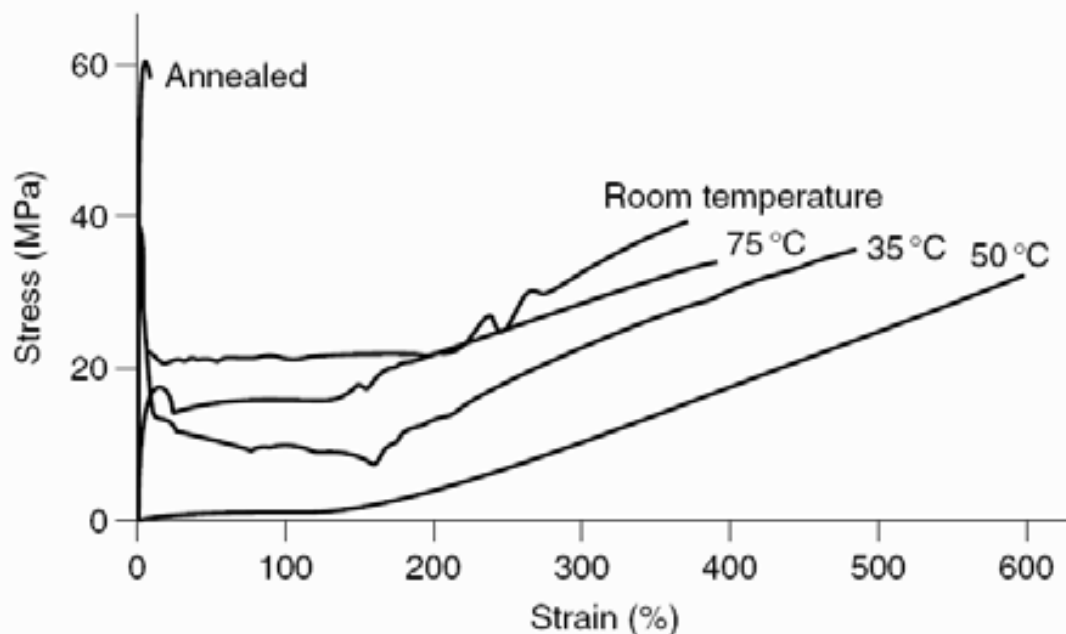
Fig. 5. PTT stress–strain curves at draw temperatures below and above the glass transition temperature [31].

This unexpected drawing behavior was due to the onset of cold crystallization competing with drawing. To draw a polymer, it is usually heated to temperatures above its T_g so that the polymer became soft to facilitate draw. However, when the polymer cold-crystallized during hot drawing, the increase in crystallinity increased the polymer's modulus and had an opposing effect to hot drawing, and therefore reduced the drawability. When cold-crystallization proceeded at a fast rate, PTT transitioned *in situ* from rubbery to ductile, such as the 75 °C draw shown in Figure 5. At higher temperatures, the polymer could become brittle and cause draw failure. Thus, PTT drawability depends on its initial thermal history and morphology, and whether it can cold-crystallize or not during hot drawing. This behavior must be taken into account in PTT fiber spinning and drawing.

3. PTT nanowire drawing

The PTT nanowire can be fabricated by using the electrospinning method reported in Ref. 32. However, the nanowire fabricated by electrospinning with large surface roughness and length inhomogeneity induces high optical loss while the PTT nanofibrous mats with diameters only 200−600 nm. The simple way to fabricate PTT wire would be direct drawing technique, which is a one-step tip-drawing process.

Figure 6 shows the schematic illustration of the drawing process. Figure 6a shows a vertical direction tip-drawing process while Figure 6b shows a random direction tip-drawing process. PTT pellets (melt temperature T_m = 225°C) was melt by a heating plate and the temperature was kept at around 250°C during the wire drawing. First, an iron or silica rod/tip with radius of about 125 μm is being approached and its tip is immerged into the molten PTT. Then the rod tip is retracted from the molten PTT with a speed of 0.1−1 m/s, leaving a PTT wire extending between the molten PTT and the tip. The extended PTT wire is quickly quenched in air and finally, a naked amorphous PTT nanowire is formed.
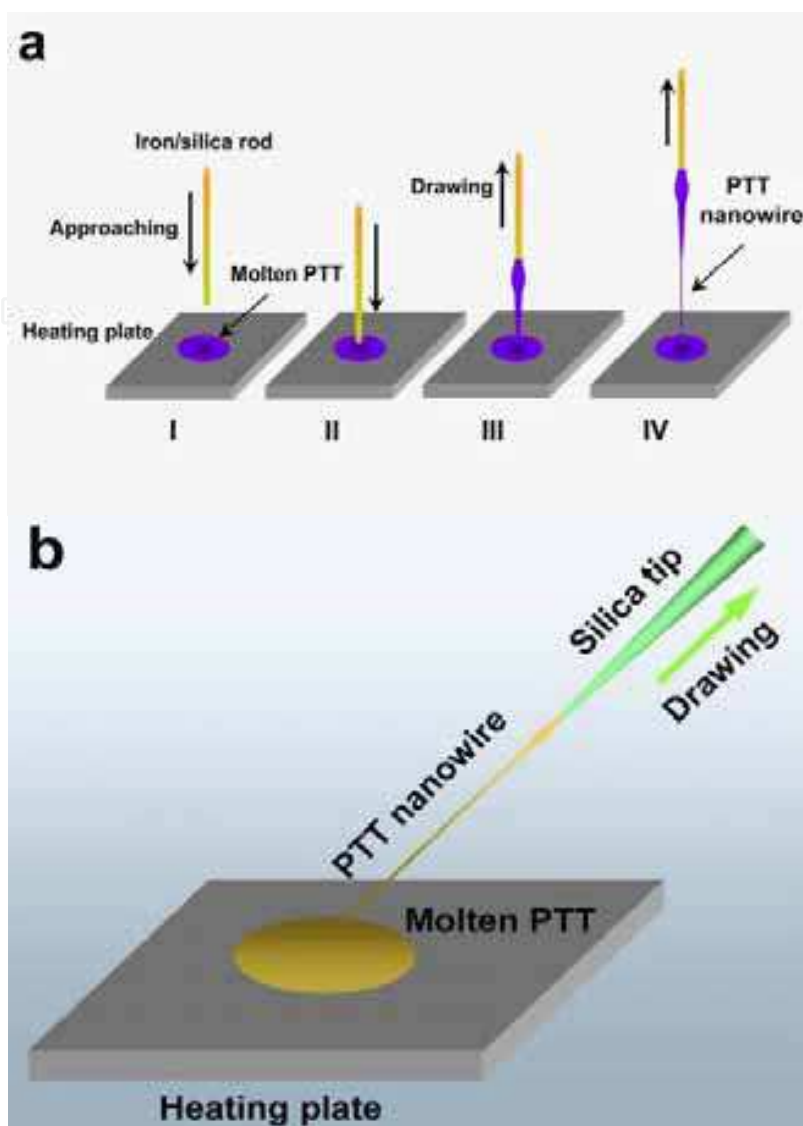
Fig. 6. Schematic illustration of nanowires fabrication by direct drawing process from PTT melt. (a) vertical direction drawing. I, An iron or silica rod is approaching the molten PTT. II, The rod end is immersed into the molten PTT. III, The rod conglutinated PTT is being drawn out. IV, A PTT nanowire is formed. (b) random direction drawing. The arrow shows the drawing direction.

4. PTT nanowire characterization

In this section, we will show the PTT nanowires by SEM/TEM images and introduce a systematic study on the dependence of nanowire evanescent wave coupling efficiency on wavelength, cross-angle, and core-diameter. Finally, optical losses of the PTT nanowires will be given, which were measured by evanescent coupling.

4.1 SEM and TEM images
To display the fabricated PTT nanowire, a 250-mm-long PTT nanowire was coiled on a 12-μm-diameter PTT bending rod. A scanning electron microscope (SEM) image (Figure 7) shows part of the coiled nanowire with a length of about 200 mm and an average diameter

of 280 nm. The diameter variation ratio is about 8.4×10^{-8}. Figure 8 show a nanowire with diameter of 105 nm.
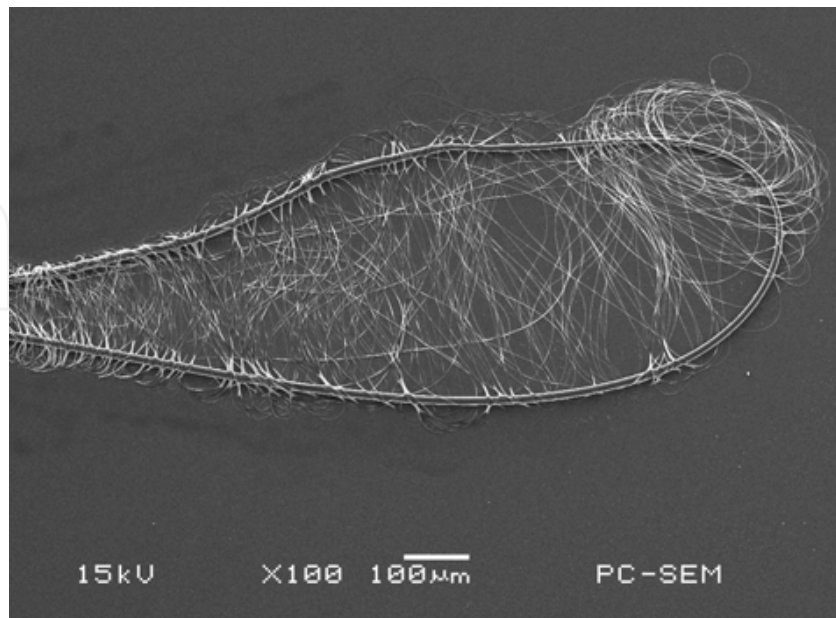

Fig. 7. SEM image of a PTT nanowire with average diameter of 280 nm coiled on a 12-µm-diameter PTT bending rod, the length of the nanowire displayed is about 200 mm.
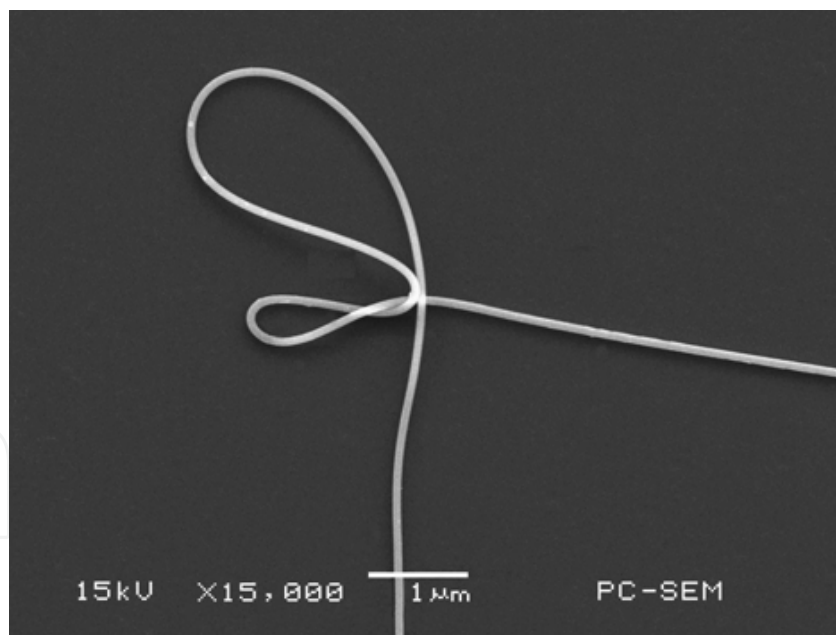

Fig. 8. 105-nm-diameter flexible nanowire rings.

For comparison, a scanning electron microscope (SEM) image (Figure 9a) shows that a 167-nm-diameter PNW with length of about 155 µm is positioned together with a 1.26-µm-diameter straight PTT rod. Figure 9b shows that four 110-nm-diameter PNWs are bent and positioned together. Figure 9c demonstrates flexible and elastic connection by pulling the PNWs with diameters of 140 and 170 nm. To examine surface roughness of the PNWs, high-magnification transmission electron microscope (TEM) was done. Figure 9d shows a TEM

image of a 190-nm-diameter nanowire, indicating no visible defect and irregularity on the surface of the PNWs. Typical average sidewall root-mean-square roughness of the PNW is 0.28 nm. The electron diffraction pattern (inset of Figure 9d) demonstrates that the obtained PNW is amorphous. The results demonstrate that the obtained PNWs exhibit high surface smoothness, length uniformity, high mechanical properties, and excellent flexibility.
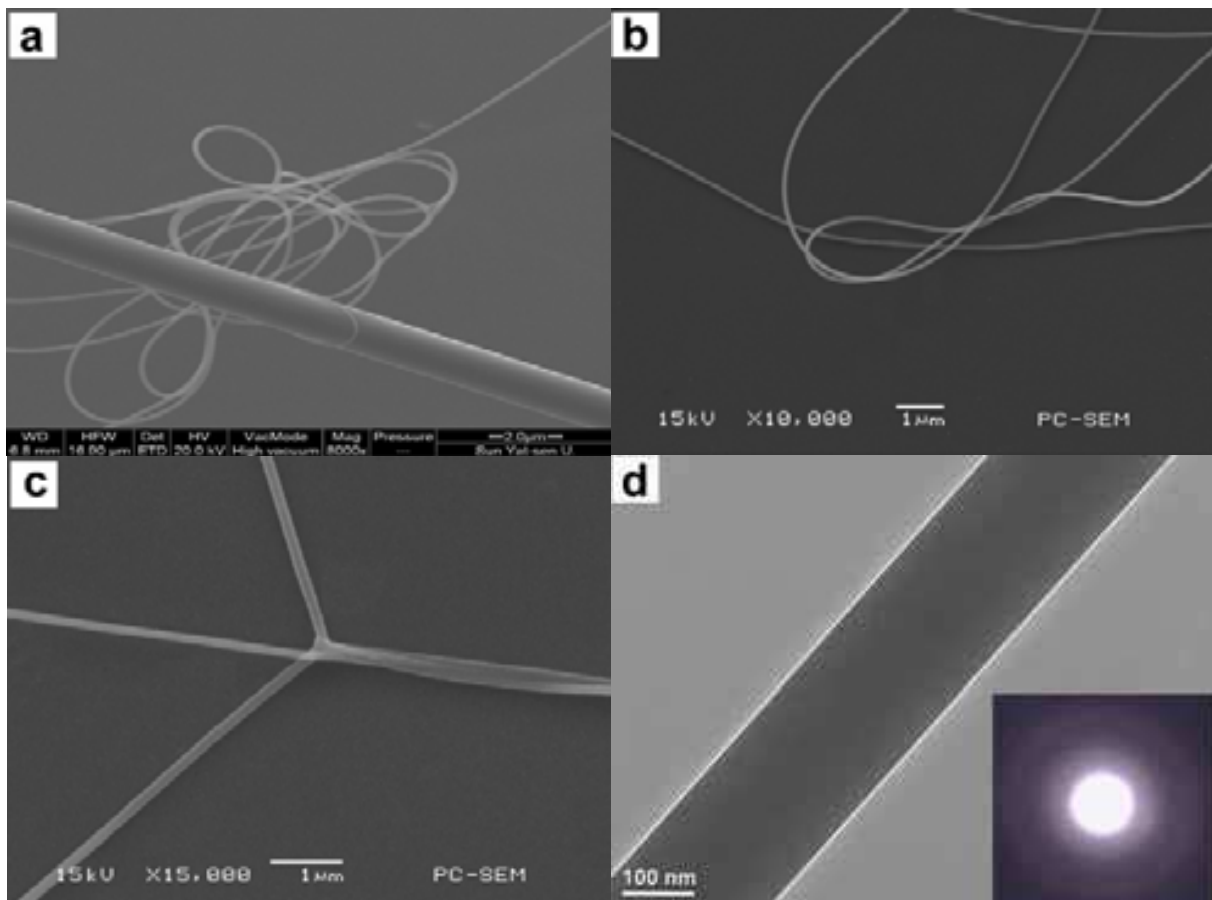

Fig. 9. Electron micrographs of PTT nanowires and nanowire structures. a–c, SEM images: (a) Comparison of a 167-nm-diameter PNW (about 155 µm long) with a 1.26-µm-diameter straight PTT rod. (b) Four 110-nm-diameter PNWs are positioned together. (c) Flexible and elastic enough PNWs connection with diameters of 140 and 170 nm. (d) TEM image of a 190-nm-diameter PNW. The inset shows its electron diffraction pattern.

4.2 Evanescent coupling [33]

In the characterization of optical nanowires, subwavelength optical wires and miniaturized photonic devices, an unavoidable issue is to launch lights of different wavelengths into them efficiently. One can use end-to-end direct optical coupling, grating coupling or evanescent wave coupling methods. The most efficient way to launch light into nanowires and nanowire-based photonic devices is evanescent wave coupling using a silica tapered fiber. However, the coupling efficiency depends strongly on the launched wavelength, the cross-angle and the core-diameter of the silica taper and the measured nanowire. In this section, we will introduce a systematic experimental study on the wavelength, cross-angle, and core-diameter dependence of coupling efficiency in nanowire evanescent wave coupling between silica tapered fiber and nanowires.

In the measurement, the PTT nanowire (PNW) was fixed by two micro-stages supports on a rotation disk by using a micromanipulator under an optical microscope. An 800-nm-diameter silica tapered fiber, which was fabricated by a direct drawing method, was fixed by a precision manipulator under an optical microscope and was used for light launching. Figure 10a shows the schematic measurement setup. When the silica tapered fiber and the PNW are close enough, they will contact each other through van der Waals and electrostatic attractive forces. In the experiment, when we rotate the disk slowly, different cross-angles between the silica tapered fiber and the PNW can be formed. The output optical power from the PNW was measured using an optical power meter. Figure 10b shows schematically the measurement of the output power at the end of the PNW.
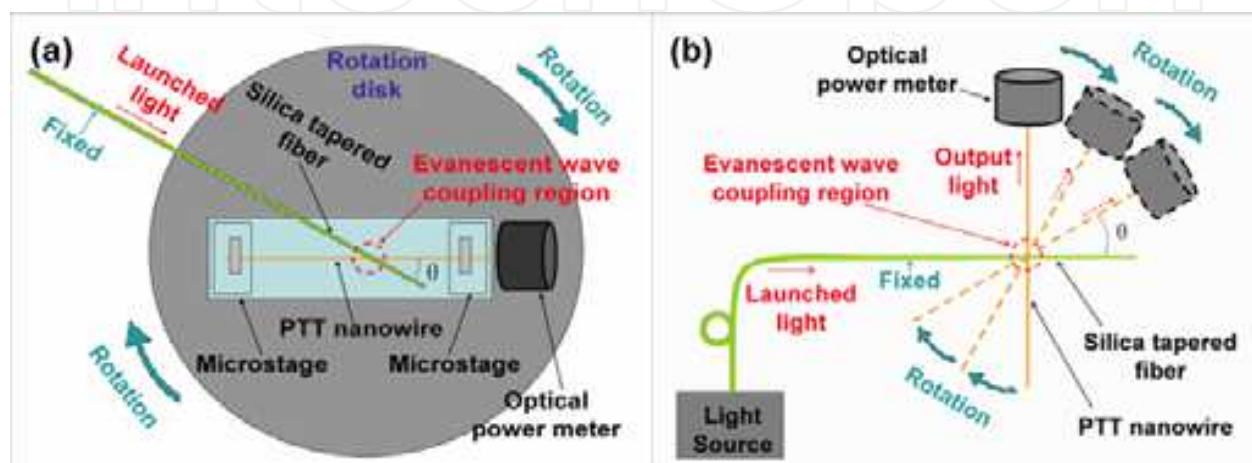

Fig. 10. Schematic diagram of the experimental setup. (a) Top view of the setup, (b) illustration of the measurement with different cross angles.

In the experiment, we first launched green (532 nm) light into a 640-nm-diameter PNW through the 800-nm-diameter silica tapered fiber, and measured the output optical power coupled into the PNW at different cross angles by rotating the rotation disk. Figure 11a shows the optical microscope images of the coupling of green light at different cross angle from 90° to 0° with a 5° changing step. It can be seen that when the silica tapered fiber (horizontal one) and the PNW crosses perpendicularly there is negligible coupling to the PNW. As a result, a bright spot is observed at the end of the silica taper with a small weak spot occurring at the cross junction. Since the cross junction under the perpendicular situation is very small, the junction can be considered as a scattering point (about 640 to 1440 nm in diameter) and there is no optical coupling. With the cross angle is decreased the measured optical power from the end of the PNW increases; the spot at the end of the silica tapered fiber becomes dark and the spot at the junction disappears gradually. This is because the cross angle is decreased the coupling strength between the silica tapered fiber and the PNW increases, and more power is coupled into the PNW through evanescent wave coupling. As a result, the bright spot at the junction gradually disappears and the optical power coupled into the PNW reaches a maximum. Similar phenomena were observed when blue (473 nm), red (650 nm), and near-infrared (1310 and 1550 nm) lights were launched.

Figure 11b shows the measured coupling efficiency versus cross-angle (θ) at different wavelengths (473, 532, 650, 1310 and 1550 nm). From Figure 11b, it can be seen that the measured coupling efficiency decreases with increasing cross-angle (θ). This is because a larger cross-angle will induce a smaller overlap length between the silica tapered fiber and the PNW, and the coupling efficiency decreases with increasing cross-angle (θ). For

example, for green (532 nm) light, at $\theta = 0°$, 63.4% optical power was coupled into the PNW from the silica taper. When $\theta = 45°$, the coupling efficiency was only 1.65%. Also, the measured coupling efficiency increases with increasing launched wavelength. This is because more optical power leaks out of the nanowire core when the launched light wavelength increases, and the leakage of the optical power enhances energy exchange between the nanowires within a short interaction length. For example, about 80% coupling
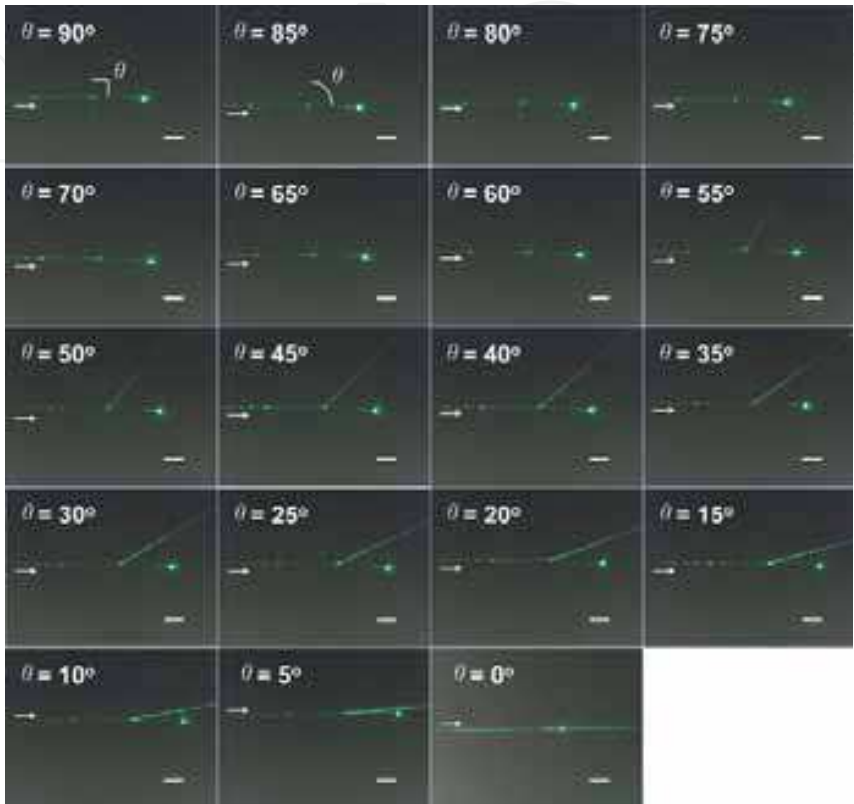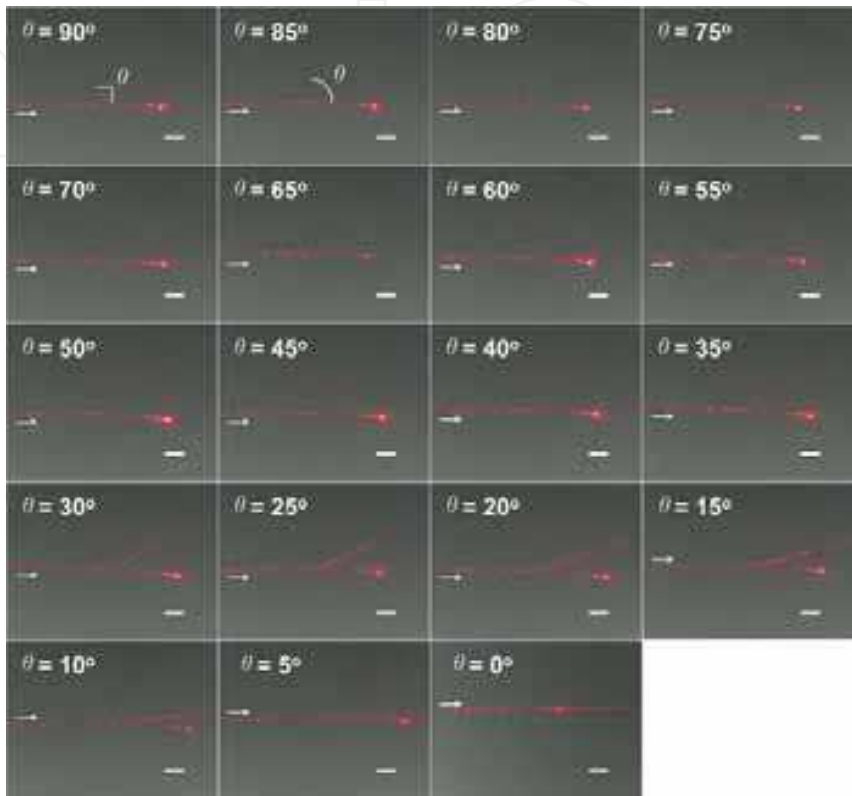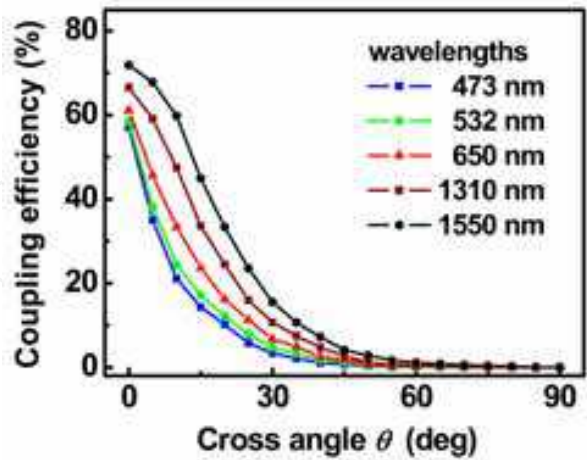

(a)
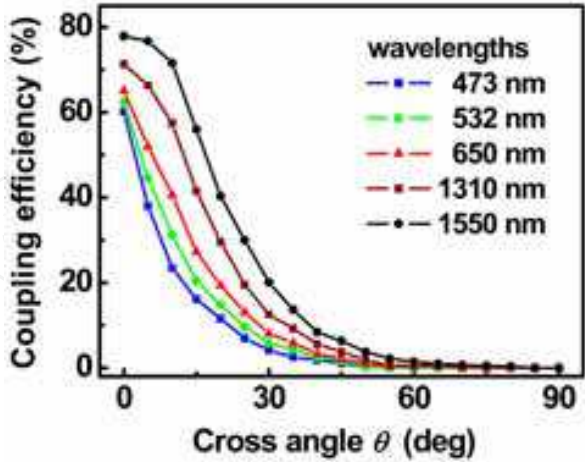
(b)

Fig. 11. (a) Optical microscope images of the evanescent wave coupling. Green (532 nm) light was launched from an 800-nm-diameter silica tapered fiber into a 640-nm-diameter PNW at different cross-angles from 90° to 0° with a 5° changing step. The white arrows show the propagation directions of the launched lights. The scale bar represents 20 µm. (b) Measured coupling efficiency versus cross-angle (θ) at different wavelengths.

efficiency is obtained for 1550 nm near-infrared light at $\theta = 0°$, and for 473 nm blue light the coupling efficiency is about 60% at $\theta = 0°$.

Similar dependence behavior of the coupling efficiency is also observed in a 790-nm-diameter PNW. Figure 12a shows red (650 nm) light was coupled from the 800-nm-diameter silica tapered fiber (horizontal) into a 790-nm-diameter PNW. Figure 12b shows the measured coupling efficiency versus cross-angle (θ) when lights with different wavelengths
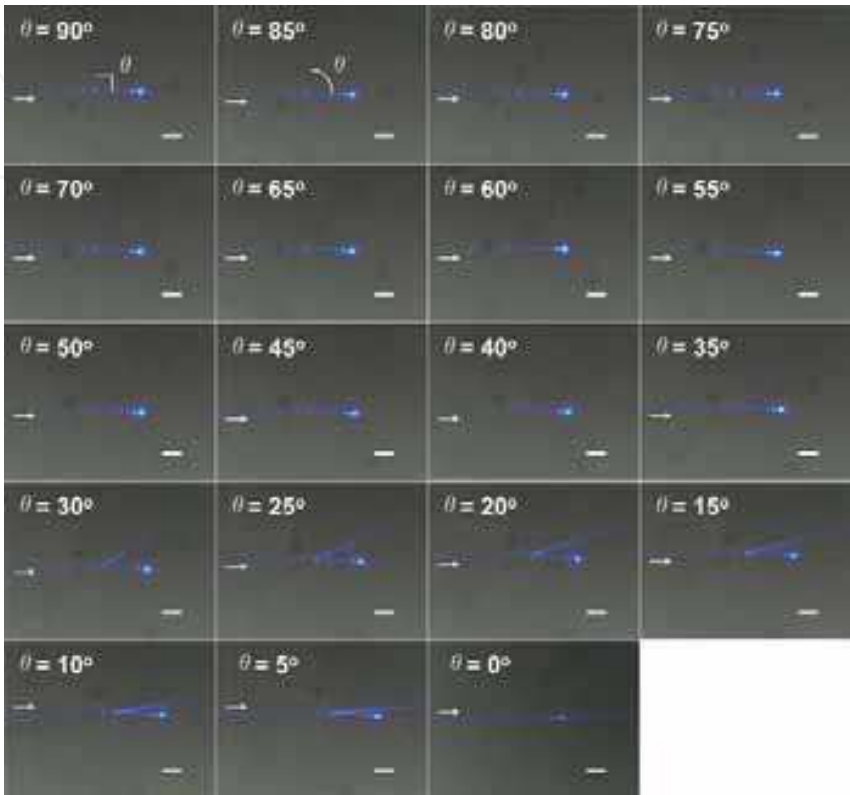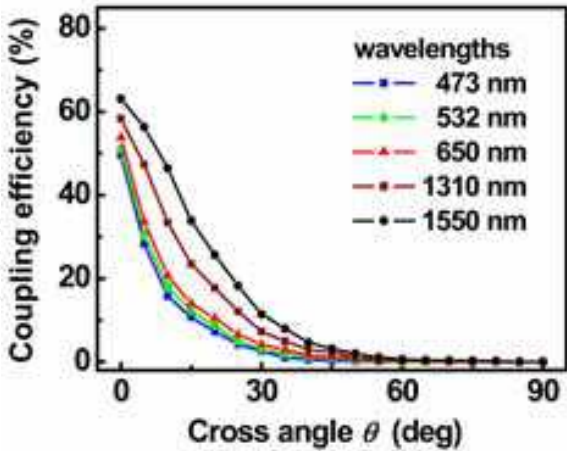

(a)

(b)

Fig. 12. (a) Optical microscope images of the evanescent wave coupling. Red (650 nm) light was launched from an 800-nm-diameter silica tapered fiber into a 790-nm-diameter PNW at different cross-angles from 90° to 0° with a 5° changing step. The white arrows show the propagation directions of the launched lights. The scale bar represents 20 μm. (b) Measured coupling efficiency versus the cross angle (θ) at different wavelengths.

(473, 532, 650, 1310, and 1550 nm) were individually launched into the 790-nm-diameter PNW. With decreasing cross-angle (θ) the output power increases. For example, taking the case if red (650 nm) light, when $\theta = 45°$, only 1.88% optical power was coupled into the PNW. When $\theta = 15°$, 24.1% optical power was coupled into the PNW. When $\theta = 0°$ the coupling efficiency reached a maximum value of 62.1%.

(a)

(b)

Fig. 13. (a) Optical microscope images of the evanescent wave coupling. Blue (473 nm) light was launched from an 800-nm-diameter silica tapered fiber into a 950-nm-diameter PNW at different cross-angles from 90° to 0° with a 5° changing step. The white arrows show the propagation directions of the launched lights. The scale bar represents 20 μm. (b) Measured coupling efficiency versus the cross angle (θ) at different wavelengths.

Figure 13a shows blue (473 nm) light coupled from the 800-nm-diameter silica tapered fiber (horizontal) to a 950-nm-diameter PNW. Figure 13b shows the measured coupling efficiency versus cross-angle (θ) when light at different wavelengths (473, 532, 650, 1310, and 1550 nm) were individually launched into the 950-nm-diameter PNW. For example, taking the case of blue (473 nm) light, when $\theta = 45°$, 21.9% power was coupled into the PNW. When $\theta = 15°$, about 10% power was coupled into the PNW. When $\theta = 0°$ the coupling efficiency reached a maximum value of 46.5%.

To investigate the core-diameter dependence, the coupling efficiency versus cross angle for different core-diameters at different wavelengths was plotted. Figure 14 shows the coupling efficiency of different nanowire diameters as a function of launched wavelength at $\theta = 0°$ and different nanowire diameters. It has been concluded that: 1) for the same cross angle and same nanowire diameter, the coupling efficiency will be higher for longer wavelength; 2) for the same wavelength and same cross angle, the coupling efficiency will be higher for smaller nanowire diameter; 3) for the same wavelength and same nanowire diameter, the coupling efficiency will be higher for smaller cross angle. As expected, to get the maximum coupling efficiency the silica tapered fiber used for light launching and the nanowire must be placed in parallel. Here it should be pointed out that, even for zero cross-angle (the two wires contacted in parallel), the coupling efficiency will be different for different overlap length.
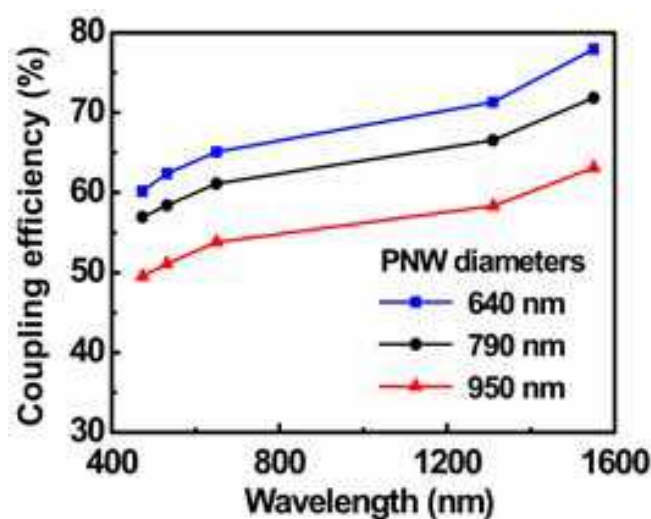

Fig. 14. Measured coupling efficiency versus different wavelengths of launched light at $\theta = 0°$ and different nanowire diameters.

4.3 Optical loss

Guided optical properties of the PTT nanowires were characterized by fixing the nanowires by two microstage supports, and launched lights of different wavelength into them by evanescent coupling through directional coupling as shown in Figure 15a. As an example, the figure shows green light (532 nm) was coupled into a 470-nm-diameter PTT nanowire bend from a submicro-taper silica fiber with a coupling length of 10.5 μm, where the upper red and yellow colors show the simulated evanescent coupling by the beam propagation method (BPM). It should be emphasized that some light scattering in the PTT nanowire was induced by surface contamination rather than surface roughness. The output powers from the PTT nanowires were measured by an optical power meter together with an optical

spectrum analyzer. The optical losses of the PTT nanowires were measured by a cutback method. In the measurement, the original nanowire we used to evaluate the loss is 5 to 20 cm. In each cutback of the measurement, about 1-mm-long fiber was cut off from the output end of the nanowire. Figure 15b shows the plots of the PTT wire diameter versus measured optical loss at the wavelengths of 473, 532, 650, 1310, and 1550 nm. The measured rate of the PTT nanowires' loss over time is 0.4 dB/hour, which is smaller than that of the silica nanowires (about 1 dB/hour). The measured coupling efficiency is as high as 95% when a silica taper is parallel to the PTT wire.
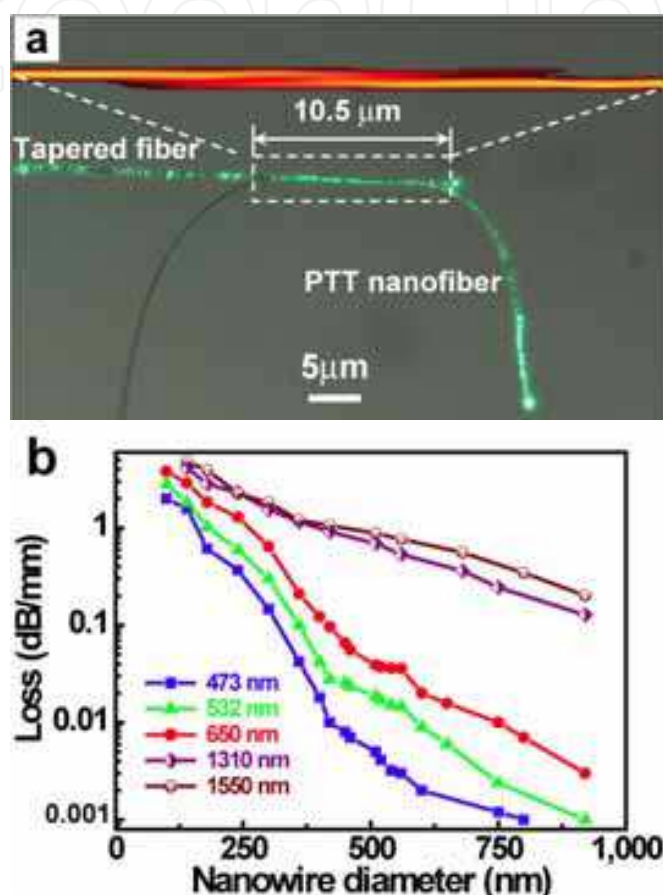

Fig. 15. Optical coupling method and the measured optical loss. (a) Optical microscope image of a tapered silica fiber launched 532 nm green light into a 470-nm-diameter PTT nanowire bend by evanescent coupling, where the coupling length is 10.5 µm. The upper red and yellow colors illustrate the coupling region simulated by the beam propagation method. (b) Optical loss of PTT wires versus different diameter at the wavelengths of 473, 532, 650, 1310, and 1550 nm.

5. Twisting method

There are several methods to assemble nanowire devices. Here we introduce a simple nanowire device assembly method, named "twisting method".

Figure 16 shows the twisting process. As an example, we use two nanowires to demonstrate the method: First, a nanowire was drawn from the PTT melt by a one-step direct drawing process and cut into two segments. Second, the two segment nanowires were placed in

parallel on two microstage supports with their ends fixed (Figure 16a). Third, we rotated the right support in anti clockwise direction with a high precision while keeping left support fixed (Figure 16b). The rotation was stopped when desirable number of turns was obtained in the twisted region (*e.g.*, four twisted turns, Figure 16c). Finally, a twisted 2 × 2 coupling device was formed.
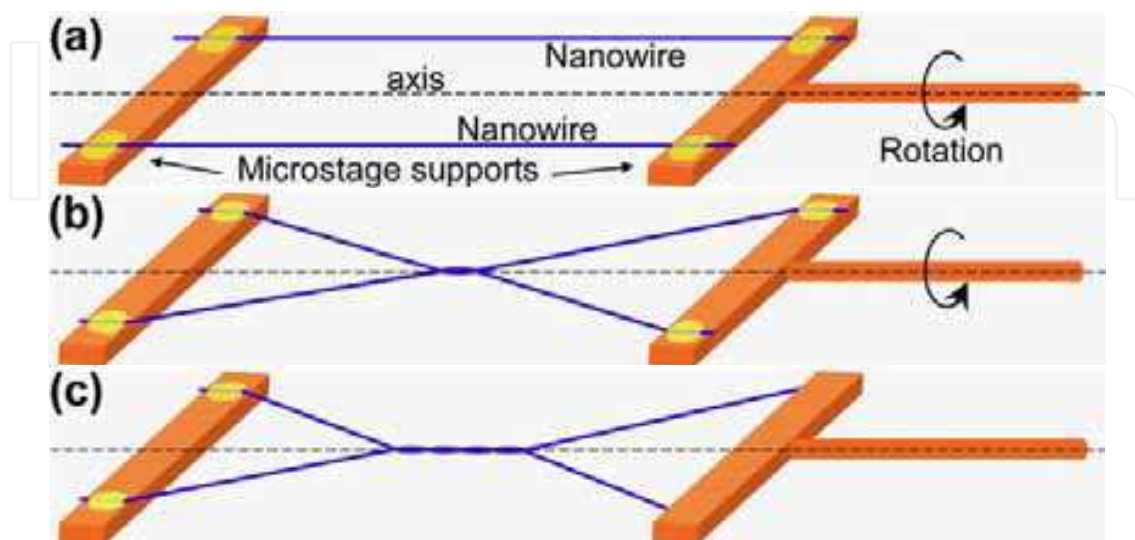

Fig. 16. (a) Two parallel PTT nanowires were fixed by two microstage supports. The left support is fixed and the right support can be rotated around the axis. (b) A twisted 2 × 2 structure with one twisted turn was formed by rotating the right support. (c) A twisted 2 × 2 structure with four twisted turns was formed by further rotating the right support.

By using the simple twisting method with microstage supports under a microscopy, any coupling device with multi-branches can be easily assembled depending on how many nanowires were used.

6. Nanodevices

6.1 SEM images of arbitrary nanodevices [34]

A series of nanodevices were assembled, as examples, Figure 17a shows a nano bird's nest (top right of the Figure). The nanowires can also be bent from 0 to 180°, as an example, Figure 17b shows a 45° bend with diameter of 280 nm while Figure 17c shows a 155° sharp bend with diameter of 160 nm. Figure 17d shows that a 340-nm-diameter nanowire was bent to a tweezer-shaped structure with a bending radius of 1.6 μm. Similarly, a 70-nm-diameter nanowire was first twisted, and then bent to form a scissor-shaped structure (Figure 17e). Figure 17f shows a 2×2 coupler with three twist turns in the coupling region by twisting 110-nm- and 150-nm-diameter nanowires.

Figure 18 shows the SEM images of some nanowire devices and device arrays. Figure 18a shows a directional coupler assembled by two parallel 750-nm-diameter nanowires with a 110 nm coupling gap. Figure 18b shows a Y-branching coupler assembled by two 360-nm-diameter nanowires without coupling gap. We further assembled a bending Y-branching coupler by a 210-nm-diameter 155° bend (inside up) and a 270-nm-diameter 120° bend (outside down) (Figure 18c), a 2×2 coupler by two 150-nm-diameter nanowires (Figure 18d), and a basic asymmetric MZ coupler by two 60-nm-diameter nanowires (Figure 18e).
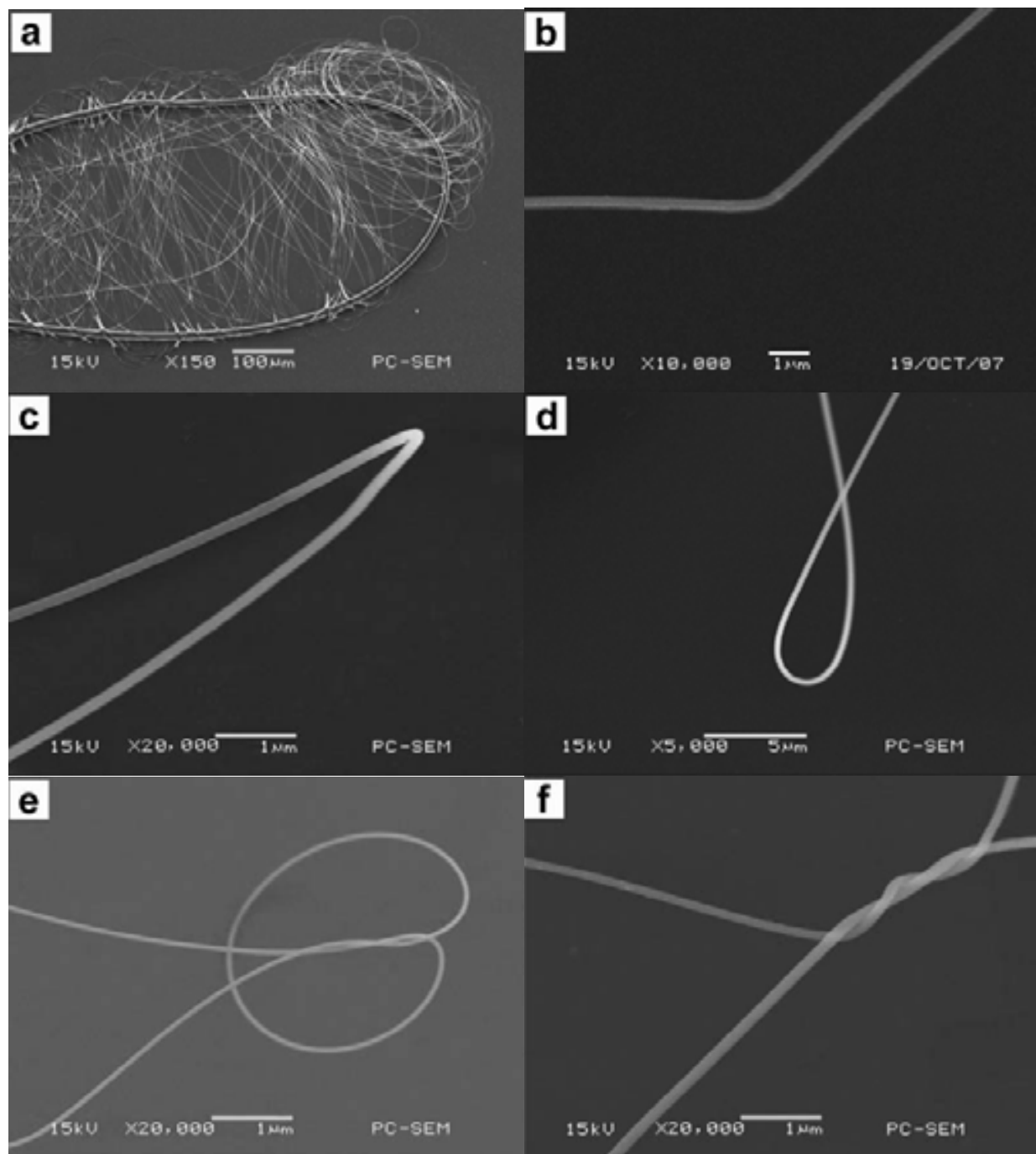
Fig. 17. Scanning electron microscope (SEM) images of nanodevices. (a) A nano bird's nest with average diameter of 280 nm on a 12-µm-diameter PTT bending rod (top right). (b) A 45° bend with a diameter of 280 nm. (c) A 155° sharp bend with a diameter of 160 nm. (d) A 340-nm-diameter tweezer-shaped nanowire. (e) A 70-nm-diameter scissor-shaped nanowire. (f) A twisted 2×2 coupler consists of 110-nm- and 150-nm-diameter nanowires.

Furthermore, integrated device arrays were constructed (Figures 18f−i), where the insets in yellow colour show their respective schematic structures. Figure 18(f) shows an integrated structure cascaded by two MZ couplers using 100-nm-diamter nanowires. Figure 18g shows an integrated device cascaded by a 2×2 coupler and a MZ coupler using 130-nm-diameter nanowires. Figure 18h shows a three inputs four outputs device array formed by two 300-

nm-diameter 2×2 couplers in parallel and, Figure 18i shows a three inputs three outputs device array formed by four X-crosses with nanowire diameter of 560 nm.
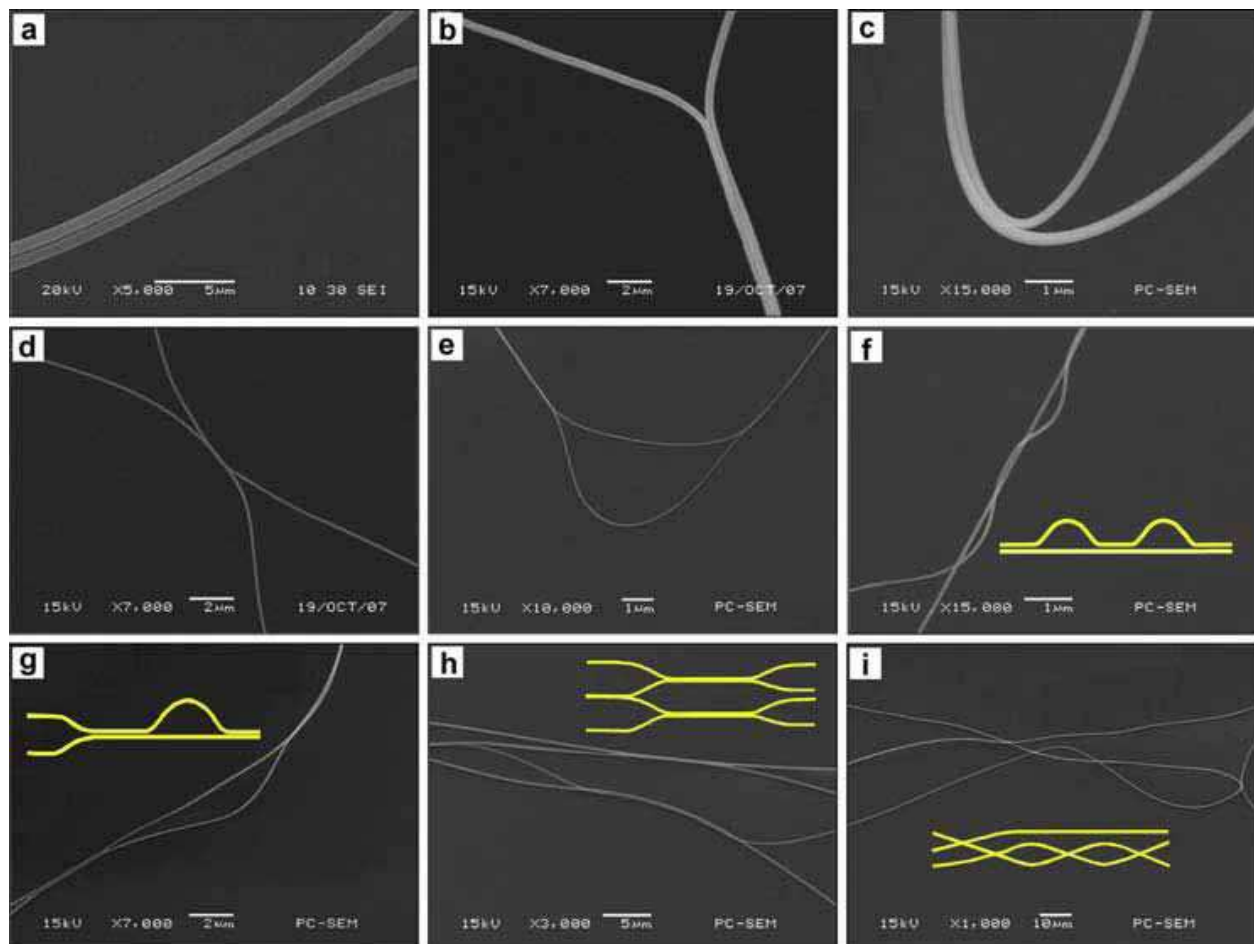

Fig. 18. SEM images of photonic devices and device arrays constructed by PTT nanowires. (a) A directional coupler with a 110 nm coupling gap between the two 750-nm-diameter nanowires. (b) A 360-nm-diameter Y-branching coupler without coupling gap. (c) A zero coupling gap coupler cascaded by a bending Y-branch (inside bend: 155°-bending-angle, 210-nm-diameter; outside bend: 120°-bending-angle, 270-nm-diameter). (d) A 2×2 coupler (150-nm-diameter). (e) A basic asymmetric MZ structure (60-nm-diameter). (f) An integrated coupler cascaded by two MZ structures (100-nm-diameter). (g) An integrated device cascaded by a 2×2 coupler and a MZ structure (130-nm-diameter). (h) A three inputs four outputs device array integrated by two 2×2 couplers (300-nm-diameter). (i) A three inputs three outputs device array integrated by four X-crosses (560-nm-diameter). The insets in yellow colour in (f)−(i) show respective schematic diagrams of the integrated structures.

6.2 Optical images of arbitrary nanodevices [34]

To analyze the optical characteristics at different wavelengths, we launched lights of different wavelengths into the assembled nanowire devices and device arrays. As an example, Figure 19a shows the launched blue light (473 nm) in the input port B is split into two parts by a 2×2 branching splitter, which was formed by twisting two 340-nm-diameter nanowires with one twist turn. The twisted region is shown in the inset of Figure 19a. The

branching angles is 25° and the splitting ratio is 46:54 for the outputs C:D. The measured insertion loss is less than 0.3 dB. We have also assembled a 1×3 branching splitter by twisting three 290-nm-diameter nanowires (Figure 19b), and coupled blue light into the input port A with a splitting ratio of about 35:40:25 (from output ports B to D) and a total insertion loss of less than 0.3 dB. Figure 19c further shows red light (650 nm) in a 1×4 branching splitter with diameter of 350nm and splitting ratio of 23:20:28:29 (from output ports B to E). The measured total insertion loss is about 0.35 dB. From Figures 19a−c, we can see that the scattering lights are extremely weak in the branching areas, which is desirable for high performance optical beam splitters/couplers. In Figure 19d, we launched red light into a 500-nm-diameter twisted spiral nanowire with a 680-nm-radius ring at its end and found that that the optical power was well confined within the fiber core. BPM analysis shows that the bending loss is about 0.15 dB through the nanoring with radius as small as 680 nm. Figure 19e shows green light in an 850-nm-radius ring with nanowire diameter of
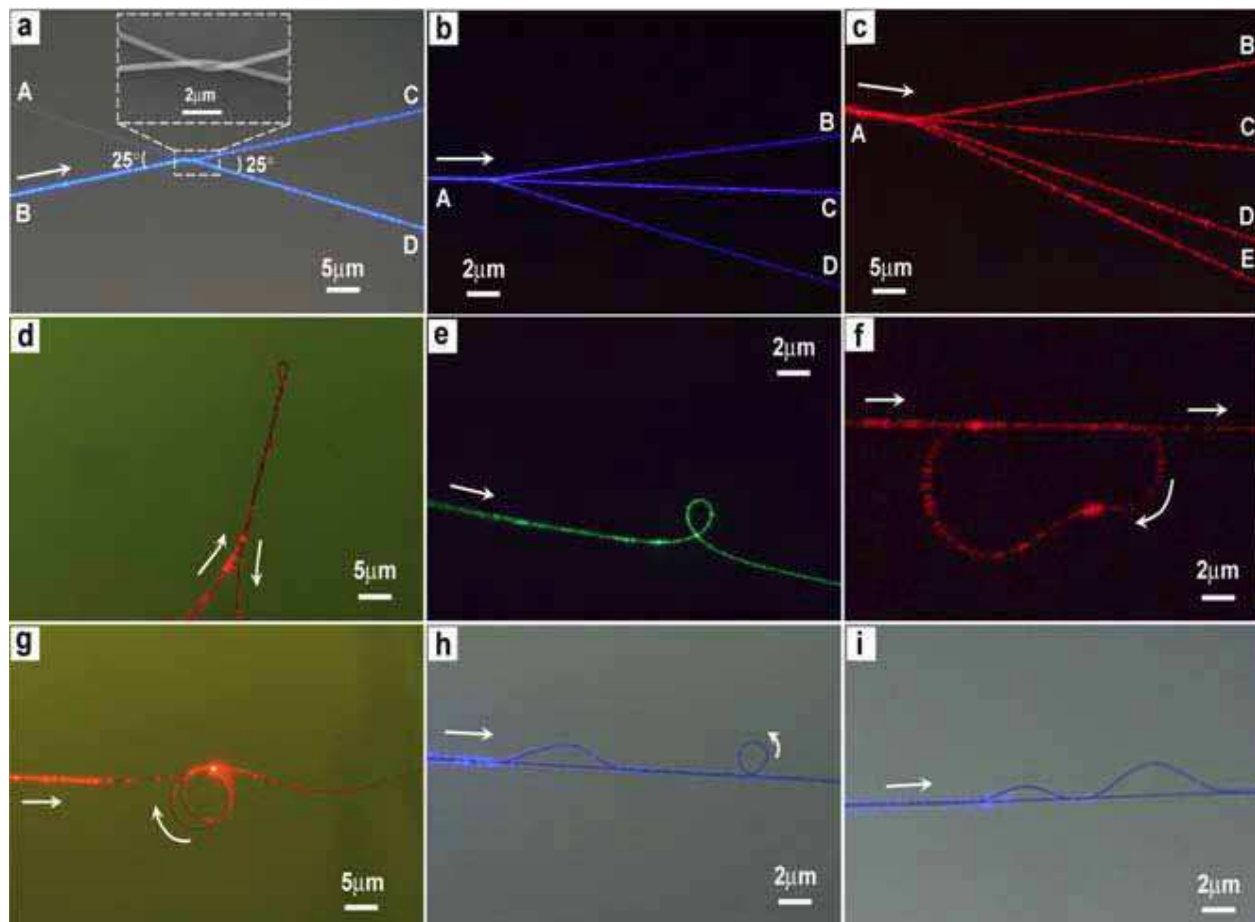

Fig. 19. Optical microscope images of the guided visible lights in different PTT nanowires and nanowire devices. (a) Blue light in a 2×2 (340-nm-diameter) branching splitter. (b) Blue light in a 1×3 (290-nm-diameter) branching splitter. (c) Red light in a 1×4 (350-nm-diameter) branching splitter. (d) Red light in a 500-nm-diameter twisted spiral nanowire with a 680-nm-radius ring. (e) Green light in an 850-nm-radius ring (120-nm-diameter). (f) Red light in a 230-nm-diameter racetrack-shaped resonator. (g) Red light in a 550-nm-diameter doubled-loop resonator (average radius about 3.8 µm). (h) Blue light in a 210-nm-diameter integrated device cascaded by a MZ structure and an 850-nm-radius ring. (i) Blue light in an integrated structure cascaded by two MZ structures (210-nm-diameter).

120 nm. The result shows that the optical field is confined in a small area of about 0.3 µm × 0.3 µm around the nanowire with good optical confinement. We have also characterized a 230-nm-diameter racetrack-shaped resonator (Figure 19f), which exhibits good transmission with an insertion loss of about 1.0 dB. In addition to above, optical microscope image of our double-loop resonator (550-nm-diameter) with an average radius of about 3.8 µm (Figure 19g) demonstrates that light can also be transmitted in multiple-rings (the measured total insertion loss is 2.4 dB). Therefore, a variety of ring-typed structures, ranging from simple fiber knot to complex coil/microcoil resonators can be achieved by proper assembling of the PTT nanowires. Figure 19h shows blue light in a 210-nm-diameter integrated structure cascaded by a basic asymmetric MZ structure and an 850-nm-radius ring. The total insertion loss is 0.38 dB. Moreover, Figure 19i shows blue light in a 210-nm-diameter integrated structure cascaded by two basic asymmetric MZ couplers with a total insertion loss of 0.33 dB. These structures demonstrate good feasibility of PTT nanowire-based integrated devices for miniaturized photonic integrated circuits.

6.3 Optical couplers and splitters [35]

A series of ultracompact photonic coupling splitters with multi-input/output ports were assembled by twisting flexible polymer nanowires. They are desirable for high density photonic integrated circuits (PICs) and nanonetworks.

Figure 20a shows SEM image of a 2×2 photonic coupling splitter with a branching angle of 25°, which was formed by twisting two polymer nanowires (PNWs) with diameters of 460 nm (branch A-1) and 548 nm (branch B-2). The inset of Figure 20a shows that there are three twisted turns in the coupling region (about 14.7 µm long and 1 µm wide). To demonstrate its optical coupling and splitting properties, we launched visible lights into different input branches by evanescent coupling. As examples, Figure 20b shows a 650 nm red light was launched into the branch A, coupled through the three-turn coupling region, and then divided into the output branches 1 and 2. Figure 20c shows a 532 nm green light was launched into the branch A, coupled through the three-turn coupling region, and then divided into the output branches 1 and 2 with a splitting ratio of about 54:46. The excess loss of the device, defined as -10log(sum[P_{output}]/P_{input}), is 0.65 dB, including 0.48 dB input and output coupling loss. The propagation loss is 0.007 dB and the scattering loss is 0.163 dB in the twisted region. Similarly, Figure 20c shows that a 473 nm blue light is divided by the device with a splitting ratio of about 60:40. The measured excess loss is 0.63 dB, which is composed of coupling loss (0.48 dB), propagation loss (0.001 dB), and scattering loss (0.149 dB). It is revealed that the device is very efficient in guiding and splitting lights. To investigate the influence of branching angle on the device performance, input/output branching angles of the splitter was changed from 8° to 90°. The calculated results show that the splitting ratios for branches 1 and 2 are ranging from 46:54 to 56:44 if a green light is launched into the branch A, and ranging from 55:45 to 62:38 if a blue light is launched into the branch B. In our experiment, we found that if the branching angles of the 2×2 splitter are 10° or 40°, a 3-dB splitter can be achieved in the case of the green light was launched into the branch A. The splitter with large branching angle operates at a large excess loss, because the bending loss and the scattering loss increase with the increase of the branching angle.

Figure 21 further shows the assembled 2 × 2 splitter (different branching angles) with visible lights in the nanowires. The diameter of the PTT nanowires is 580 nm and the branching angles of the splitter are 37° and 45°. There is one twisted turn (about 2 µm long) in the coupling region. The coupling region (one twisted turn) of the splitter is 1.16 µm wide
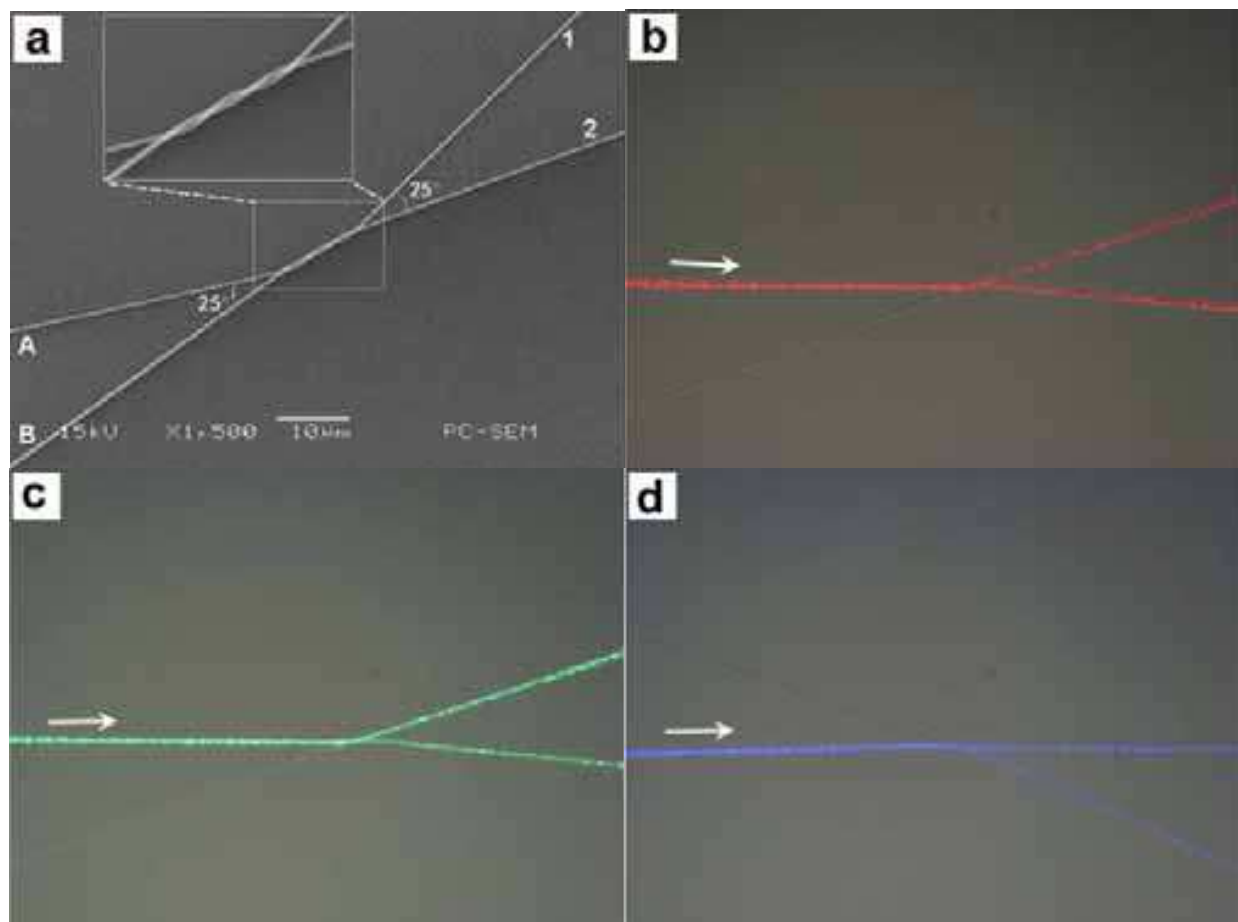
Fig. 20. A 2×2 photonic coupling splitter. (a) SEM image of the splitter with diameters of 460 and 548 nm for branches A-1 and B-2, respectively. (b)-(d) Optical microscope images of the guided red (650 nm), green (532 nm) and blue (473 nm) lights, respectively. The arrows show the propagation directions of the launched lights.

and about 2 µm long. Figure 21a shows a 650 nm red light launched into the input branch B, coupled through the one-turn coupling region, and then divided into the output branches C and D with a splitting ratio of about 40:60. Figure 21b shows that a 532 nm green light is divided by the device with a splitting ratio of about 45:55. Figure 21c shows a 473 nm blue light divided into branches C and D with a splitting ratio of about 40:60. The excess loss of the splitter is 0.63 dB. We also launched the visible lights into the input branch A of the splitter, the measured respective splitting ratios are 60:40 (red), 58:42 (green), and 50:50 (blue), the measured excess loss is 0.635 dB.

To observe the influence of the branching angles on the splitting properties of the device, the branching angles of the 2 × 2 splitter were changed to 44° and 38°. Figure 22 shows the guiding optical images of the device when red, green, and blue lights are coupled into the input branch A. The measured splitting ratios are listed in Table 2. The measured excess loss is 0.60 to 0.65 dB. By comparison the splitting properties of the 2 × 2 splitters, we found that the splitting ratios are different when the operating wavelengths or the branching angles are changed. This is because that of the coupling conditions is different in the coupling region when the operating wavelengths or the input/output branching angles are changed. For a fixed wavelength, desirable splitting ratios from 0 to 100% would be achieved by changing the branching angles.
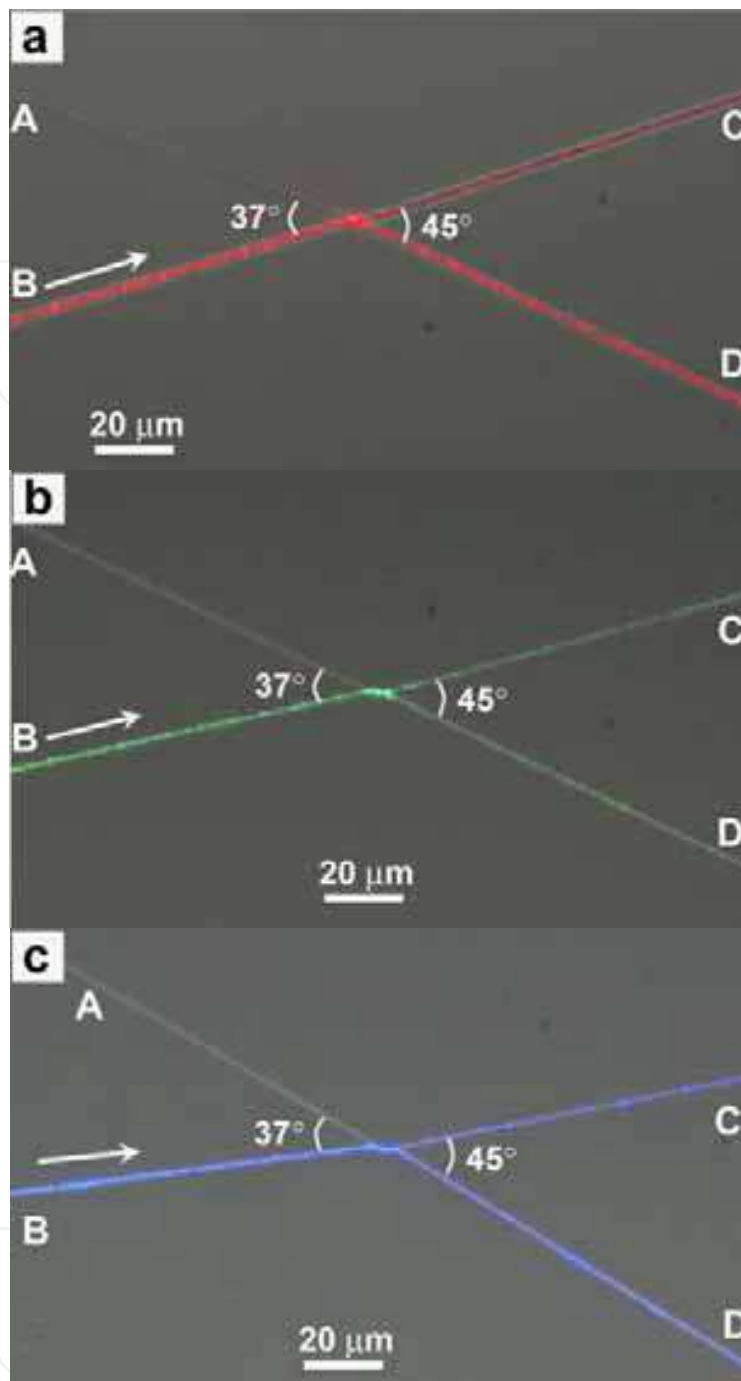
Fig. 21. Optical microscope images of the guided visible lights in the 2 × 2 optical beam splitters with branching angles of 37° and 45°. The diameter of the nanowires is 580 nm. The arrows show the propagation directions of the launched lights with (a) 650 nm red light, (b) 532 nm green light, and (c) 473 nm blue light.

Figure 23 shows a 3 × 3 optical beam splitter, which was assembled by twisting three 410-nm-diameter PTT nanowires. The length (L) of the coupling region is about 12-µm long and the width is 1.23 µm. Figure 23a shows blue light is launched into the branch A and divided into three parts, with a splitting ratio of 50:30:20 for the output branches 1 to 3. If blue light is launched into the branch B (Figure 23b), the splitting ratio is changed to be 30:40:30. When

blue light is launched into the branch C (Figure 23c), the splitting ratio is 25:38:37. We also launched the blue light into the branches B and C. The measured excess losses are 0.72, 0.61, and 0.68 dB for the input branches A, B, and C, respectively. Table 3 lists the corresponding splitting ratios of the 3 × 3 optical beam splitters at different wavelengths.
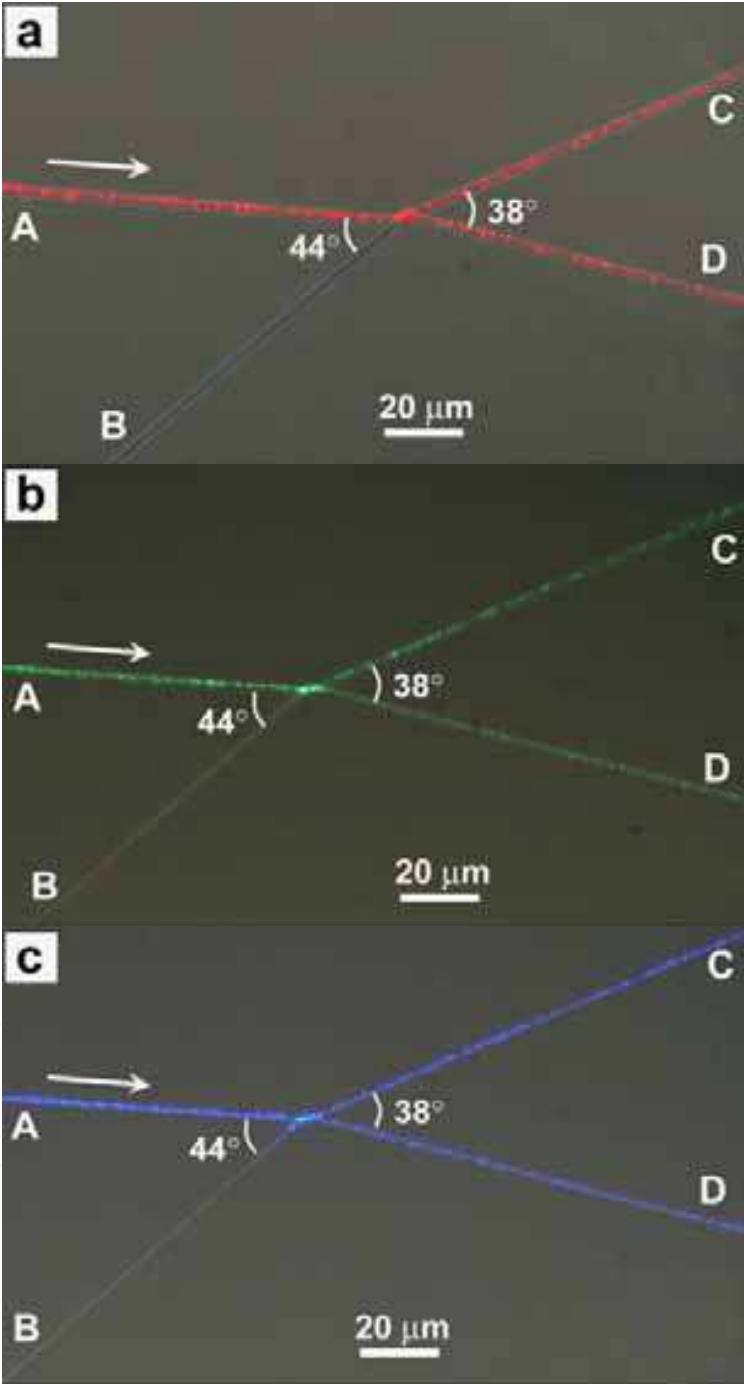

Fig. 22. Optical microscope images of the guided visible lights in the 2 × 2 optical beam splitters with branching angles of of 44° and 38°. The diameter of the nanowires is 580 nm. The arrows show the propagation directions of the launched lights with (a) 650 nm red light, (b) 532 nm green light, and (c) 473 nm blue lights.

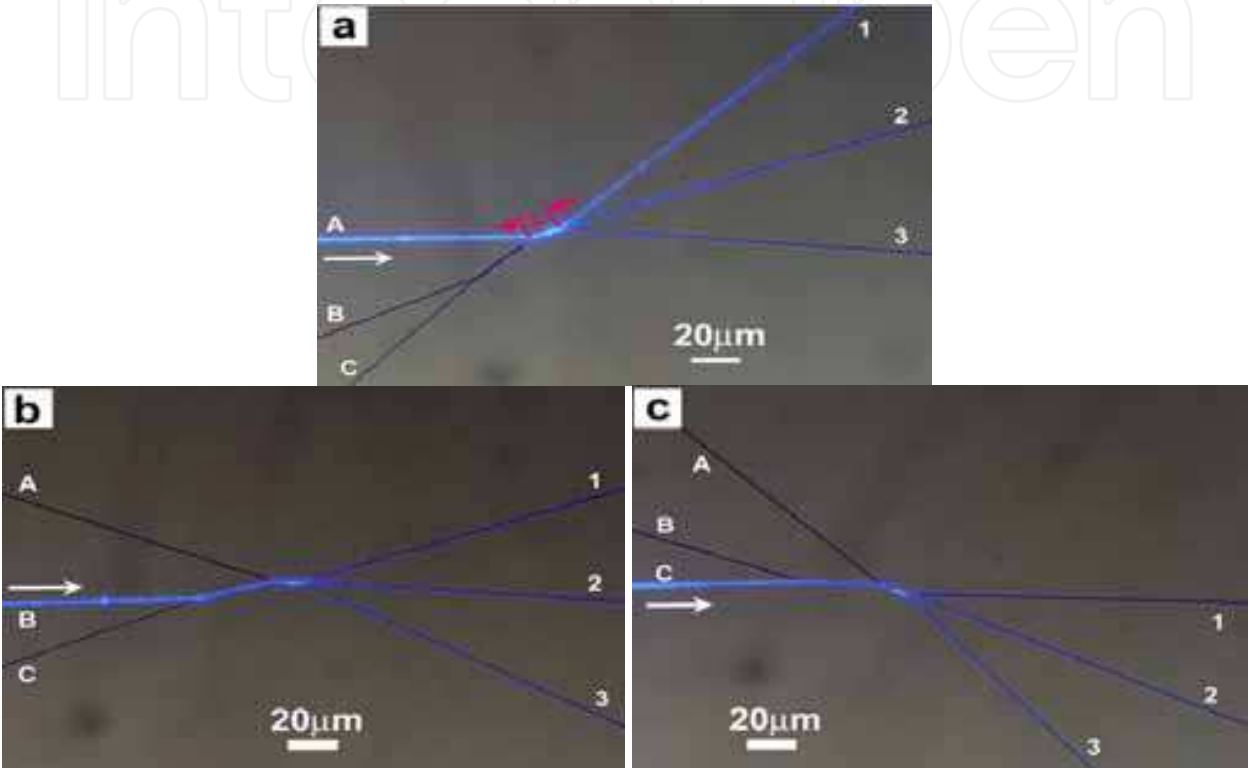| Branching angles	Input branch	Splitting ratio (C : D)		
		Red light	Green light	Blue light
37° and 45°	A	60:40	58:42	50:50
	B	40:60	45:55	40:60
44° and 38°	A	50:50	55:45	52:48
	B	50:50	51:49	42:58

Table 2. Splitting ratios of the 2 × 2 optical beam splitters

Fig. 23. Optical microscope images of the guided blue lights in a 3 × 3 optical beam splitter (410-nm-diameter). The arrows show the propagation directions of the launched blue light.

Input branch	Splitting ratio (1 : 2 : 3)		
	Red light	Green light	Blue light
A	50:25:25	55:25:20	50:30:20
B	31:38:31	32:36:32	30:40:30
C	35:33:32	32:34:34	25:38:37

Table 3. Splitting ratios of the 3 × 3 optical beam splitters

Figure 24a shows a 4×4 photonic coupling splitter assembled by twisting four PNWs with diameters of 450, 450, 510, and 570 nm for branches A to D. The inset of Figure 24a shows that the coupling section is composed of a 3×4 and a 1×4 couplers, where the total width of the coupling section is 1.98 μm. The maximum length of the coupling region (Figure 24a, inset) is about 16.1 μm, and that of the 1×4 splitter is about 8.5 μm. Figure 24b shows that a 650 nm red light is sent into the branch B and divided into the output branches 1 to 4 with a splitting ratio of about 24:25:32:19. Figures 24c and 24d show lights are simultaneously launched into the branches A and B with a power ratio of about 1:2.
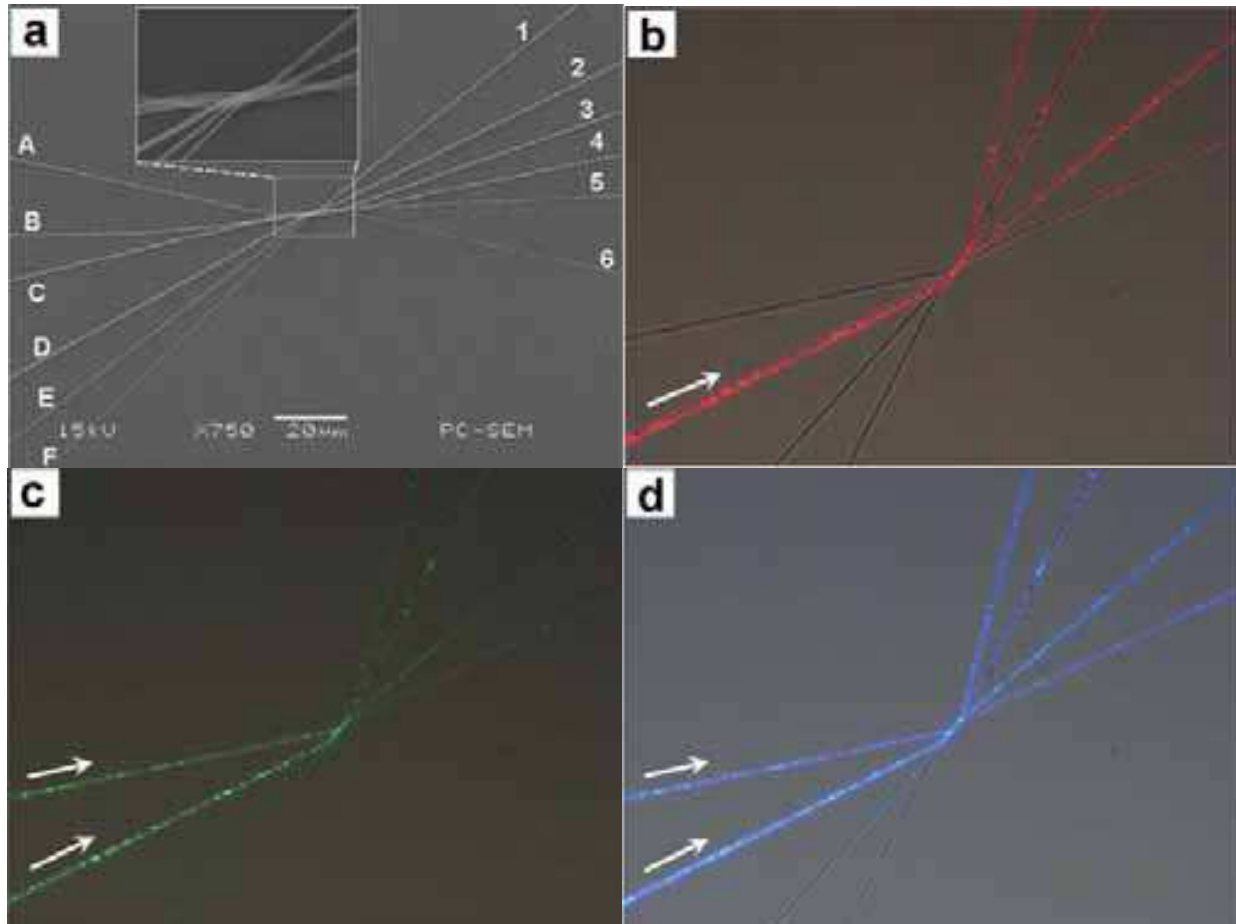
Fig. 24. A 4×4 photonic coupling splitter. (a) SEM image of the device with diameters of 450, 450, 510, and 570 nm for branches A to D. (b)-(d) Optical microscope images of the guided red, green and blue lights. The arrows show the propagation directions of the launched lights.

Figure 25a further shows a 6×6 photonic coupling splitter, which was formed by twisting six PNWs with diameters of 520, 540, 540, 540, 420, and 360 nm for branches A to F, respectively. The inset of Figure 25a shows the magnified twisted section with a coupling length of 11 to 20 µm and a coupling width of 2.92 µm. Figure 25b and 25c show red and green lights were launched into the branch C and divided into six parts, respectively. When blue light is launched into the branch D (Figure 25d), the device exhibits good power distribution uniformity and its power uniformity is about 0.03 dB. Different visible lights were also launched into the branches C and D.

An 8×8 photonic coupling splitter (Figure 26) with a longer coupling region was further assembled by twisting eight PNWs with diameters of 400, 400, 400, 400, 400, 750, 750, and 600 nm from branches A to H. The coupling section of the splitter (Figure 26a, inset) is 38-µm-long and 2.5-µm-wide. Here we launched visible lights into the device to observe the splitting phenomenon. Figures 26b and 26c show that red light is coupled into the branches E and G, respectively, and divided into branches 1 to 8. Figure 26d shows that blue light is coupled into the branch G and divided into branches 1 to 8.
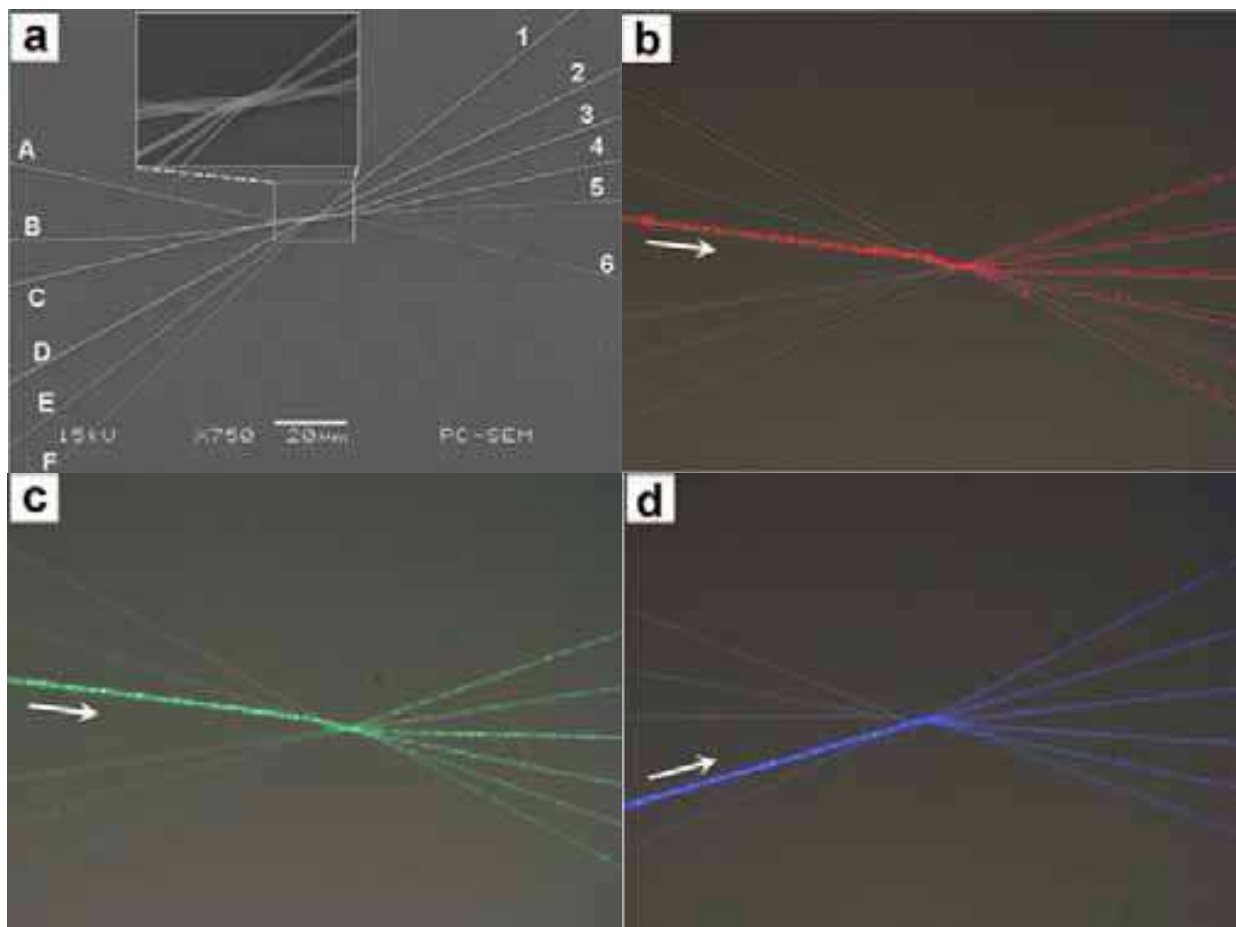
Fig. 25. A 6×6 photonic coupling splitter. (a) SEM image of the device with diameters of 520, 540, 540, 540, 420, and 360 nm for branches A to F. (b)-(d) Optical microscope images of the launched red and green lights from the input branch C, and blue light from the input branch D are split into six parts, respectively. The arrows show the propagation directions of the launched lights.

Using the facile twisting technique, $M×N$ photonic coupling splitters can be fabricated. As examples, in the following, we demonstrate 2×4, 3×3, and 5×5 photonic coupling splitters. Figure 27 shows that visible lights are coupled into a 2×4 coupling splitter with diameters of 330, 330, 330 and 320 nm for the right branches 1 to 4. The length of the twisted section is about 30 μm. The input branch B was formed by twisting three 330-, 330-, and 320-nm-diameter PNWs. Figure 27a shows that the red light is coupled into the branch A and split into four parts through the coupling region, with a splitting ratio of 26:26:26:22 for output branches 1 to 4. Figures 27b and 27c show that the green and blue lights launched from the branch B are divided into the branches 1 to 4 with splitting ratios of 30:21:20:29 and 26:25:25:24, respectively.

Figure 28 further shows a 3×3 coupling splitter cascaded by a 1×3 and a 2×3 coupling splitters, with diameters of 550, 530, and 480 nm for branches 1 to 3. The length of the coupling region of the 1×3 splitter is about 23 μm, and that of the 2×3 splitter is about 95 μm. The measured splitting ratios are 42:30:28 and 30:33:37 for output branches 1 to 3 when red (Figure 28a) and blue (Figure 28b) lights are launched into the branch A, respectively. The excess losses are 0.725 and 0.662 dB.
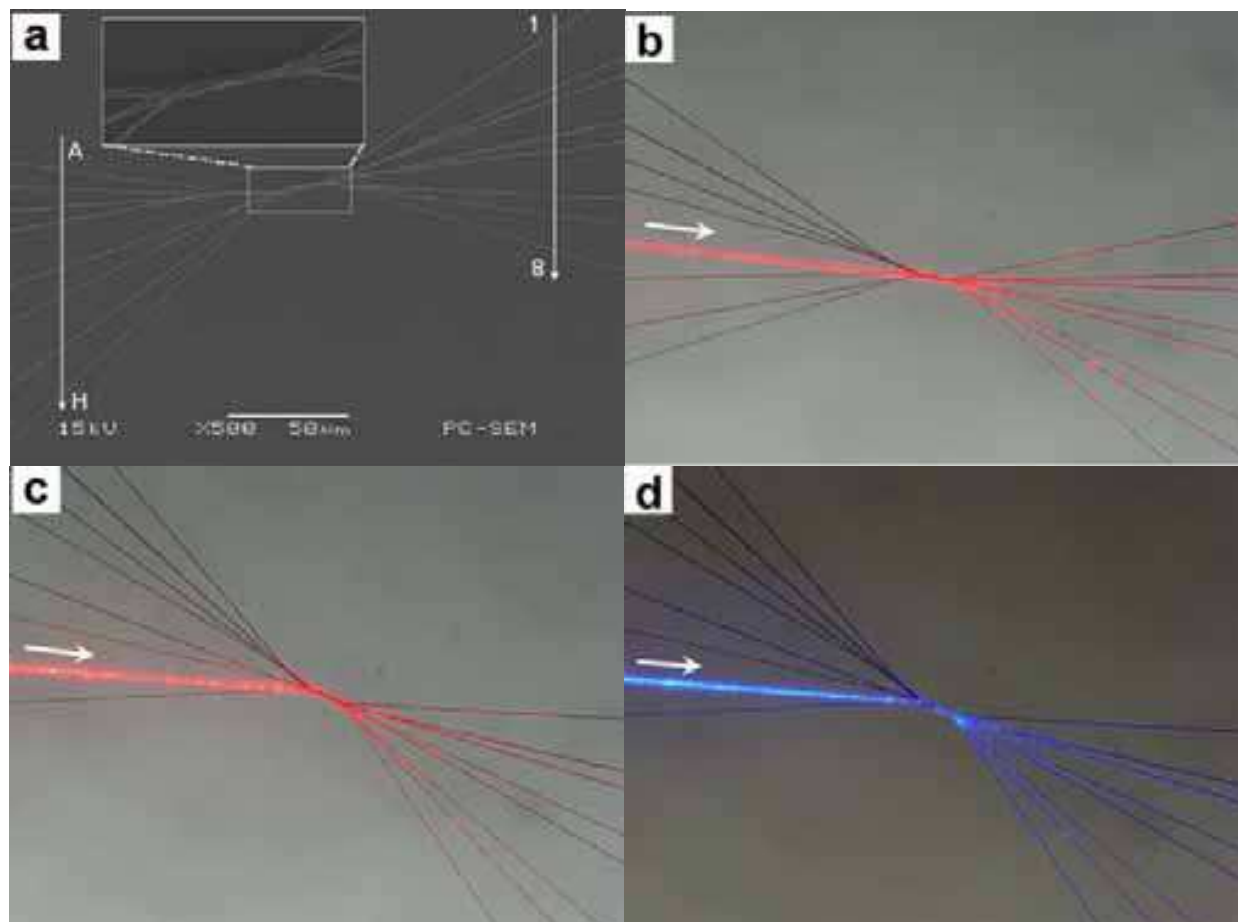
Fig. 26. An 8×8 photonic coupling splitter. (a) SEM image of the device with diameters of 400, 400, 400, 400, 400, 750, 750, and 600 nm for branches A to H. (b)-(d) Optical microscope images of the guided red and blue lights, respectively. The arrows show the propagation directions of the launched lights.

Figure 29a shows that red light is launched into the branch D of a 5×5 splitter, which was assembled by twisting five PNWs with diameters of 410, 450, 470, 470 and 470 nm for branches 1 to 5. The splitting ratio is 16:17:24:23:20 for the branches 1 to 5 and the excess loss is 0.775 dB. Figure 29b shows a 5×5 coupling splitter with diameters of 480, 450, 350, 380 and 400 nm for branches 1 to 5. Green light is launched into the branch B and split into five parts with a splitting ratio of 55:20:10:9:6 and an excess loss of 0.765 dB. Figure 29c shows that blue lights are simultaneously launched into the branches A, B, and C of a 5×5 coupling splitter, which was assembled by twisting five PNWs with diameters of 420, 540, 410, 550 and 570 nm for branches 1 to 5. The measured splitting ratio is 15:23:16:25:21 for branches 1 to 5 and the excess loss is 0.68 dB.

6.4 Interferometers [36]
Optical interferometers assembled is one of important applications of nanowires. To ensure the PTT wires used for assembly of interferometers have same diameter, a PTT wire was cut into two segments. In device assembly, the two segment wires were placed on a glass substrate, which was supported by a micromanipulator with a high precision. The first segment wire was formed to an S-shaped bend under an optical microscope. The second segment wire was pulled straight and moved to approach the S-shaped one. When the two
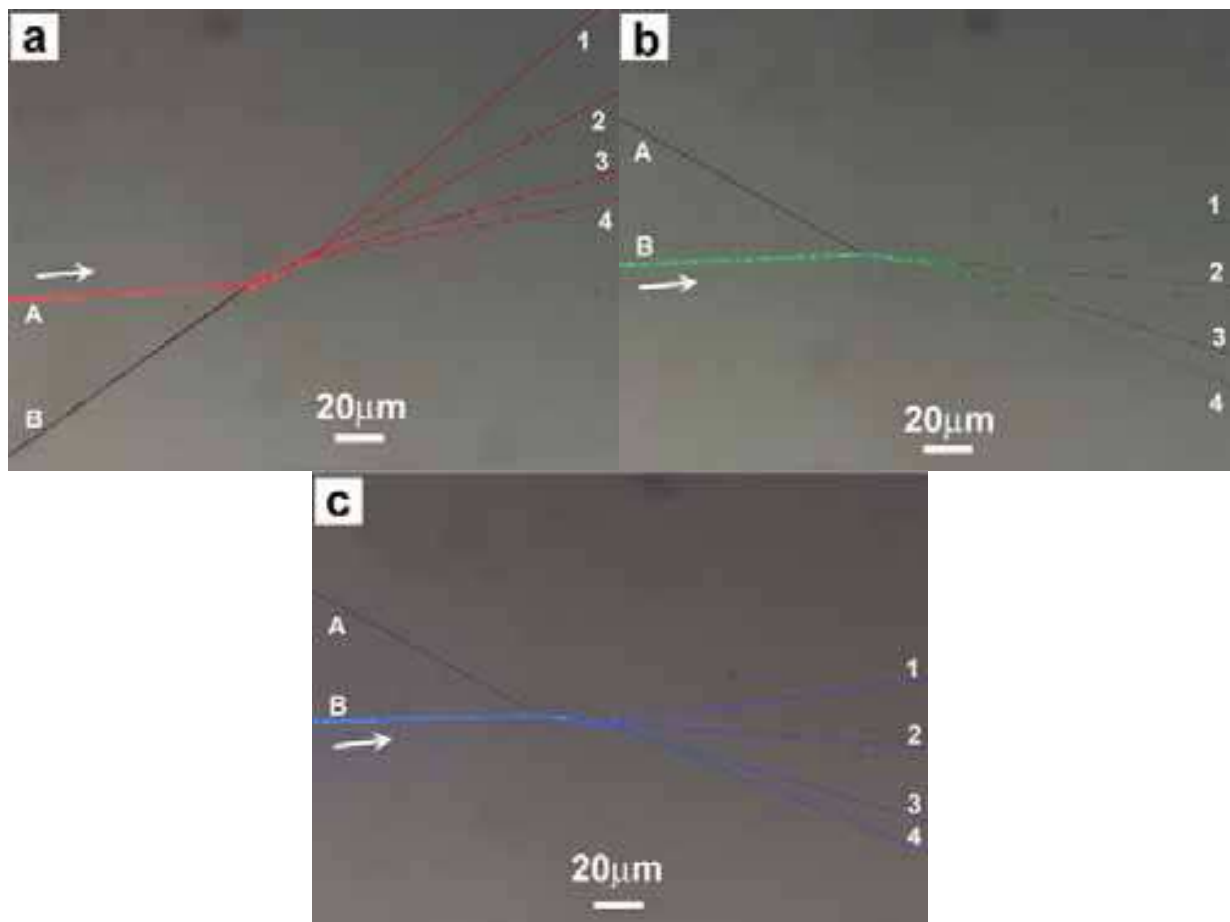
Fig. 27. A 2×4 photonic coupling splitter. The diameters of the PNWs are 330, 330, 330 and 320 nm for right branches 1 to 4. Three PNWs with diameters of 330, 330, and 320 nm are twisted together to form the left input branch B. (a)−(c) Optical microscope images of the guided red, green, and blue lights, respectively. The arrows show the propagation directions of the launched lights.

wires were close enough, they attracted each other and formed into couplers because of van der Waals force. Finally, by careful adjustment, a desired cascaded Mach–Zehnder interferometer (MZI) was assembled. The whole structure was placed on a glass substrate and the device shape is stable. Figure 30 shows a schematic diagram of the cascaded MZI. It consists of two bow-shaped MZIs (MZI 1 and MZI 2). By adjusting the contacting length between each bow-shaped bending wire and the straight wire, the lengths of the couplers (C_1, C_2, and C_3) and path-length difference (ΔL) of each bow-shaped MZI can be changed to the desired ones.

Figure 31 shows an optical microscope image of the assembled two-cascaded MZI (wire diameter, 900 nm). The inset (a) shows a scanning electron microscope image of MZI 1 and the inset (b) shows guided red light (650 nm) in the cascaded MZI. The measured insertion loss is about 0.94 dB for the red light. The total length of the cascaded MZI is 327 μm. The width and length of each bow-shaped MZI are 32 μm and 121 μm, respectively. According to the analysis, to get coupling ratios of 0.147, 0.501, and 0.147, the lengths of the couplers C_1, C_2, and C_3 are 27, 31, and 27 μm, respectively. The estimated total path-length difference is 40 μm. The bright spot in the inset (b) of Figure 31 is the scattering spot of the input light at the end of the tapered fiber I.
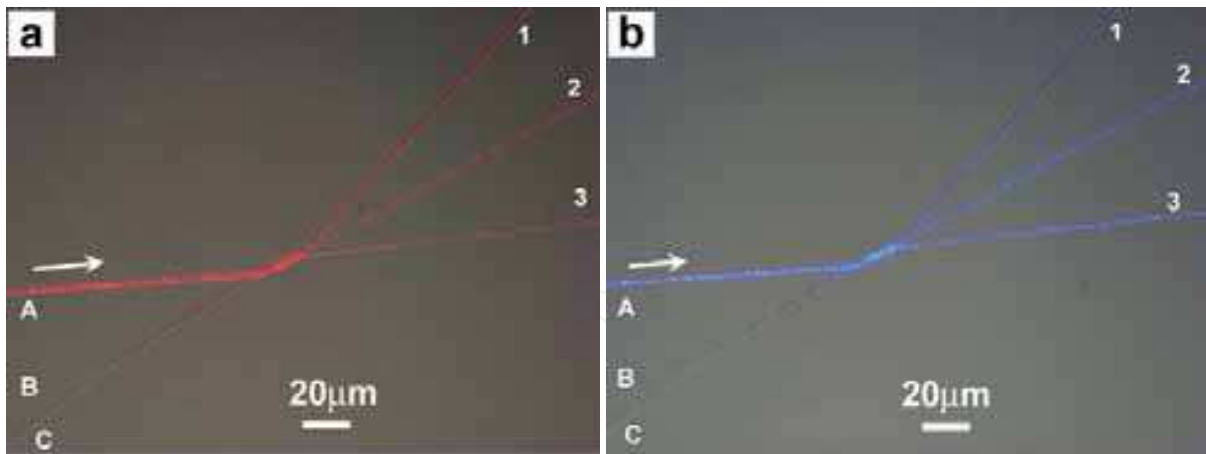
Fig. 28. Optical microscope images of the guided red and blue lights in a 3×3 photonic coupling splitter cascaded by a 1×3 and a 2×3 coupling splitters. The diameters of the PNWs are 550, 530, and 480 nm for branches 1 to 3. The arrows show the propagation directions o the launched lights.
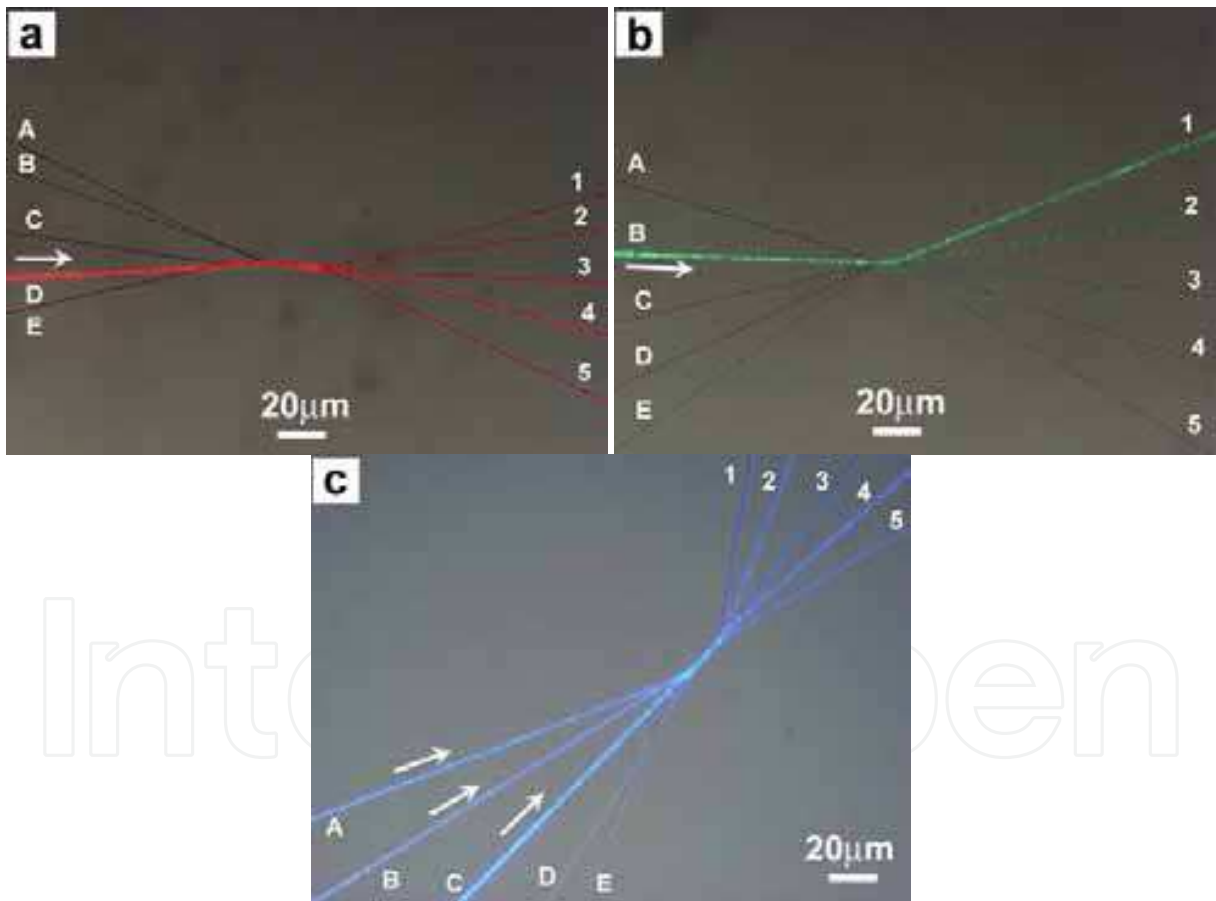

Fig. 29. Optical microscope images of three 5×5 photonic coupling splitters. (a) Red light is launched into the branch D of a 5×5 splitter with diameters of 410, 450, 470, 470 and 470 nm from branches 1 to 5. (b) Green light is launched into the branch B of a 5×5 splitter with diameters of 480, 450, 350, 380 and 400 nm from branches 1 to 5. (c) Blue lights are simultaneously launched into the branches of A, B, and C of a 5×5 splitter with diameters of 420, 540, 410, 550 and 570 nm from branches 1 to 5. The arrows show the propagation directions of the launched lights.
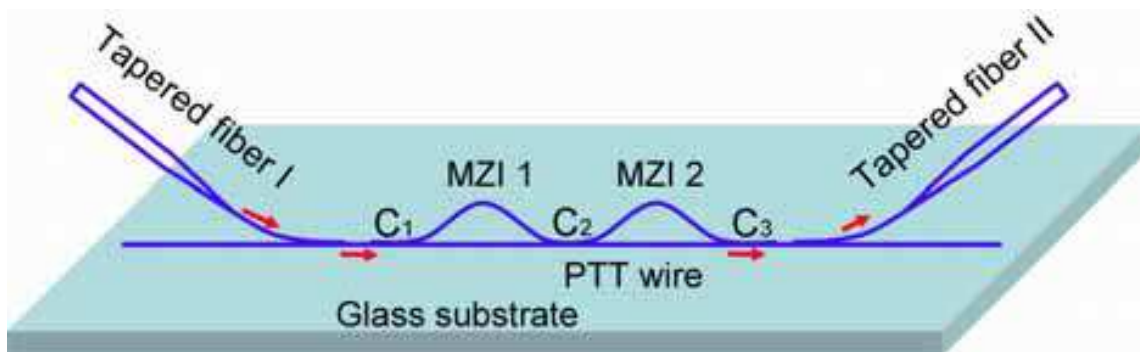
Fig. 30. Schematic diagram of a cascaded MZI. It is assembled by two PTT wires with same diameter and consists of bow-shaped MZI 1 and MZI 2. Tapered fibers I and II are used to launch and collect light by evanescent coupling. The red arrows indicate transmission direction of the light.
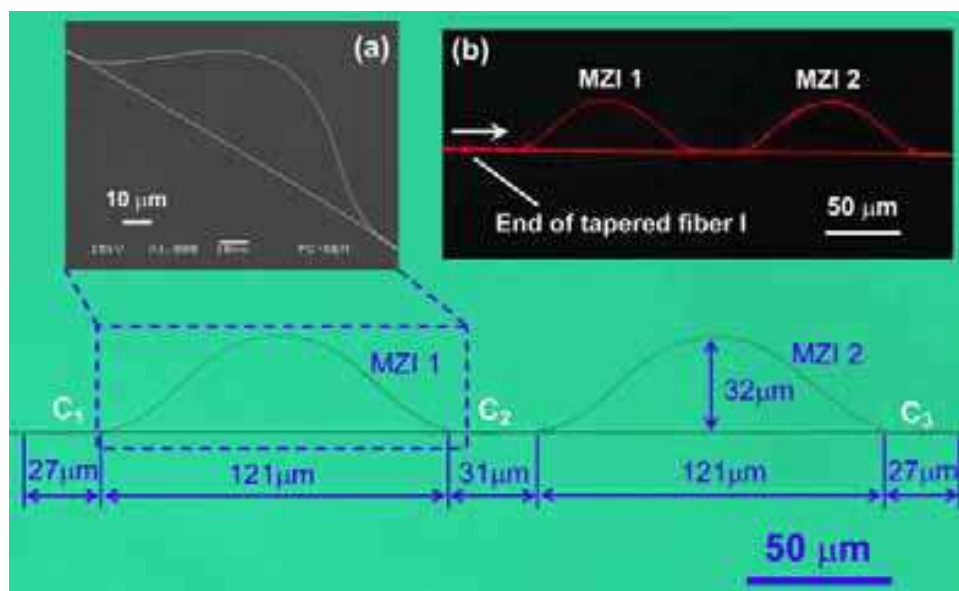

Fig. 31. Optical microscope image of the assembled cascaded MZI (wire diameter, 900 nm). Inset (a) shows the scanning electron microscope image of bow-shaped MZI 1 and inset (b) shows the optical microscope image of guided red light (650 nm) in the cascaded MZI. Estimated path-length difference is 40 µm. The white arrow in the inset (b) indicates propagation direction of the light.

Figure 32 shows the measured transmission spectrum (red dot-line) versus near-infrared wavelengths of the two bow-shaped MZI. For comparison, transmission spectrum of single bow-shaped MZI was also measured by repositioning the tapered fiber II to the straight branch of MZI 2, and depicted in Figure 32 (black dot-line). According to the curves of Figure 32, the calculated path-length differences are 21 and 42 µm for the single bow-shaped MZI and the cascaded MZI, respectively. This is well consistent with the estimated value of 40 µm for the cascaded MZI from Figure 31. The measured peak/valley ratio at the top region of the spectrum for the cascaded MZI is 1.3 to 1.7 dB. A broad pass-band appears at the top of the curve (red dot-line) and the band edge becomes sharper by using the cascaded MZI. Compared with the bandwidth (24 nm) of the single MZI, the average bandwidth of 3-

dB pass-band is improved to 33 nm for the cascaded MZI over the wavelengths of 1.3 to 1.6 µm. This is good for band-pass filter applications. The measured extinction ratio for the cascaded MZI is 16 to 19 dB, which has an improvement of 5 to 6 dB compared with the single MZI (11 to 13 dB). The measured optical insertion loss is 1.1 to 1.8 dB at wavelengths of 1.3 to 1.6 µm.
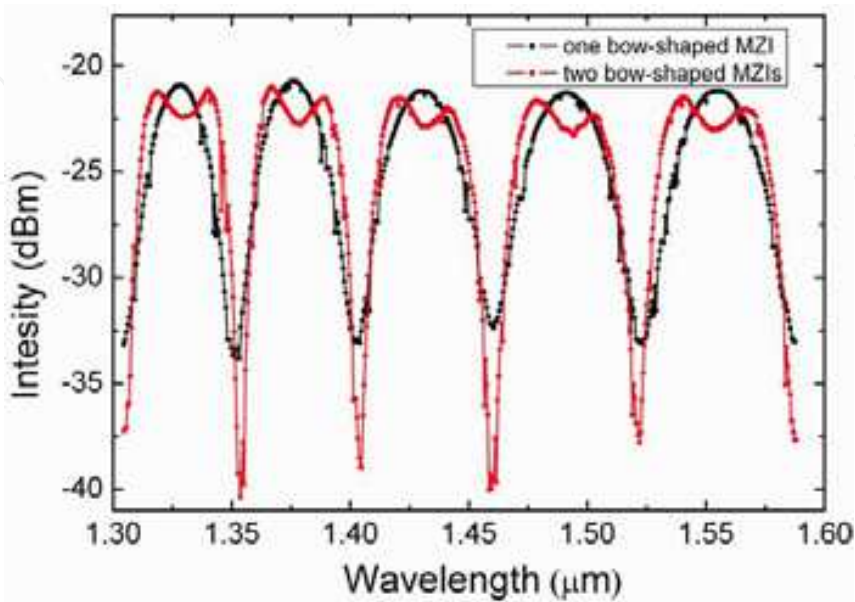

Fig. 32. Transmission spectrum versus near-infrared wavelengths. The black dot-line is the spectrum of the single bow-shaped MZI whereas the red dot-line is the spectrum of the cascaded MZI (two bow-shaped MZIs). The calculated path-length differences, from the curves, are 21 and 42 µm for the single MZI and the cascaded MZI, respectively.
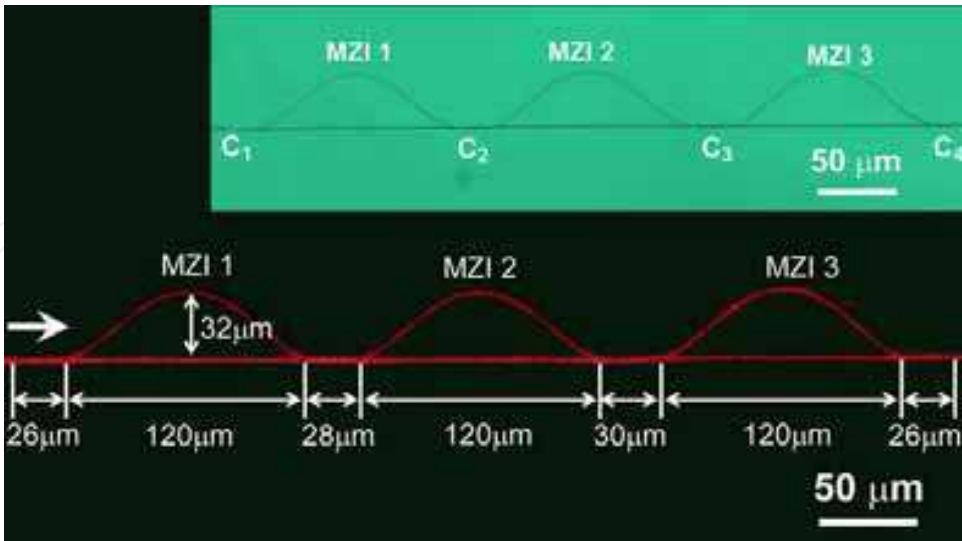

Fig. 33. Optical microscope image of the guided red light (650 nm). The inset shows the original optical microscope image of the MZI (900-nm-diameter). The estimated total path-length difference is about 61.5 µm. The white arrow indicates propagation direction of the light.

To further improve extinction ratio of the device, a cascaded MZI with three bow-shaped MZIs was assembled by two 900-nm-diameter PTT wires. Figure 33 shows an optical microscope image of the guided red light in the cascaded MZI. The measured insertion loss is 1.15 dB for the red light. The inset shows its original optical microscope image. According to the analysis, to get coupling ratios of 0.050, 0.188, 0.388, and 0.050, the lengths of the couplers C_1, C_2, C_3, and C_4 are 26, 28, 30, and 26 µm, respectively. The size of each bow-shaped MZI is 120 µm long and 32 µm wide. Total dimension of the cascaded MZI is 470 µm × 32 µm. Estimated total path-length difference for the cascaded MZI is 61.5 µm. Figure 34 shows its transmission spectrum (blue dot-line). The curve in black dot-line depicts the spectrum of the single bow-shaped MZI. From Figure 34, we calculated that the total path-length difference is 64 µm, which agreed with the estimated value of 61.5 µm. The peak/valley ratio of the cascaded MZI at the top region of the spectrum is 0.9 to 1.6 dB. The measured total insertion loss for the cascaded structure is 1.5 to 2.3 dB at wavelengths of 1.3 to 1.6 µm. The measured extinction ratio is 23 to 25 dB, which has an improvement of 12 to 13 dB compared with the single MZI (11 to 12 dB). The top region of its band-pass is wider and its band edge becomes sharper. The average bandwidth of the 3-dB band-pass for the three-cascaded MZI is 33 nm.
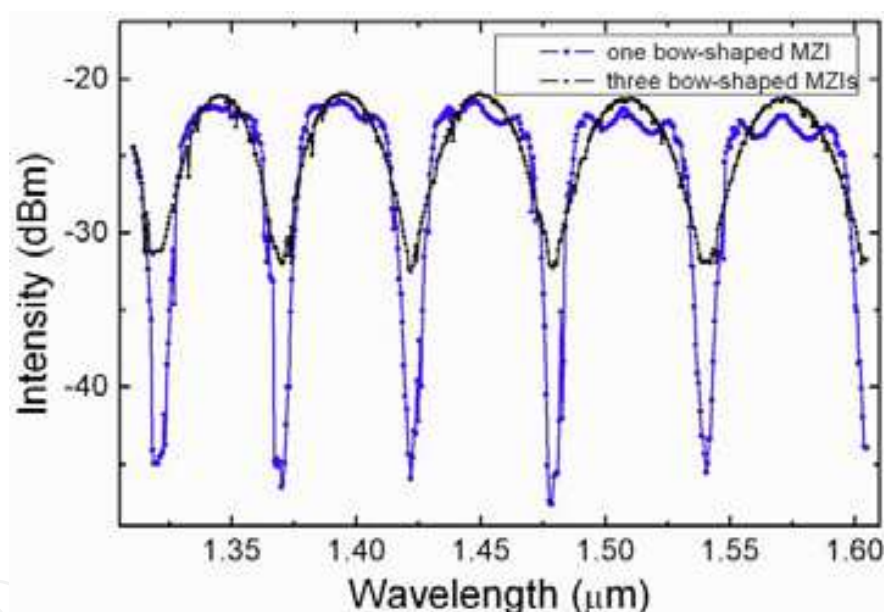

Fig. 34. Transmission spectrum versus near-infrared wavelengths. The black dot-line is the spectrum of the single bow-shaped MZI whereas the blue dot-line is the spectrum of the cascaded MZI (three bow-shaped MZIs). The total path-length difference of the cascaded MZI calculated from the spectrum is 64 µm.

In conclusion, the interferometers have a large extinction ratio with a flat-top transmission over a wide wavelength range of 1.3 to 1.6 µm. The average 3-dB bandwidth for the cascaded MZIs is broadened to 33 nm compared with the bandwidth (24 nm) of the single MZI. The extinction ratio and the measured insertion loss are 16 to 19 dB and 1.1 to 1.8 dB for the two-cascaded MZI, respectively. For the three-cascaded MZI, the measured insertion loss is 1.5 to 2.3 dB and the extinction ratio is improved to 23 to 25 dB. By carefully adjusting the bending radius of the bow-shaped MZIs (also coupling length of the PTT wires), the path-length difference could be easily controlled and the output light intensity could be tuned.

6.5 Nanosensors [37]

Nanosensor, as a promising application of nanowires, have been widely investigated. In the section, we report a tunable refractive index sensor with ultracompact structure in a 2 × 2 PTT nanowire coupling splitter assembled by twisting two flexible PTT nanowires. The sensor consists of two input branches, a twisted coupling region, and two output branches. The sensor consists of two input branches, a twisted coupling region, and two output branches, which were assembled by a simple twisting method with microstage supports
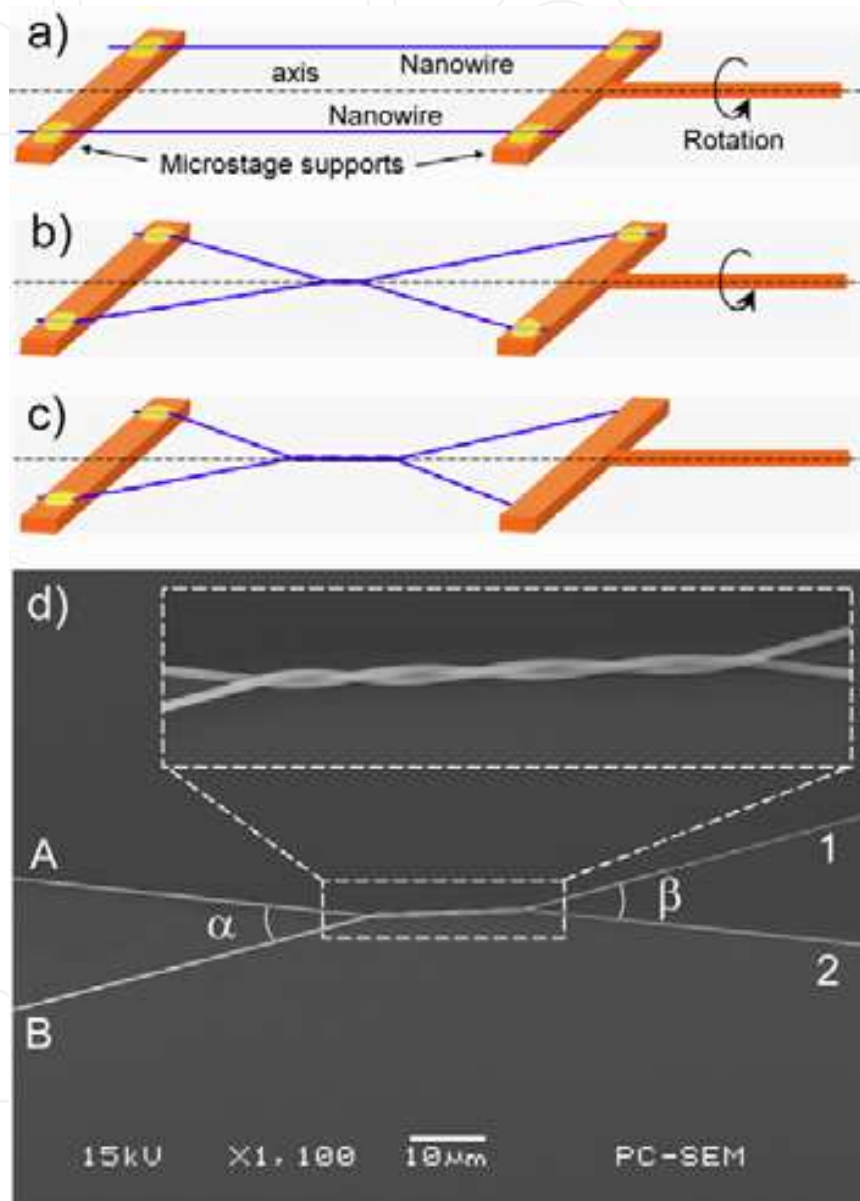

Fig. 35. Fabrication process of the PTT nanowire-based tunable refractive index sensor. (a) Two parallel PTT nanowires were fixed by two microstage supports. The left support was fixed and the right support can be rotated around the axis. (b) A twisted 2 × 2 coupling sensor with one twisted turn was formed by rotating the right support. (c) A twisted 2 × 2 coupling sensor with four twisted turns was formed by further rotating the right support. (d) SEM image of the 2 × 2 coupling sensor, which was assembled by twisting two 440-nm-diameter PTT nanowires. The inset shows the twisted region with four twisted turns. The branching angles α and β are 20°.

under a microscopy. Figure 35a–c shows assembly process of the sensor. Figure 35d shows a scanning electron microscope (SEM) image of the 2 × 2 coupling sensor with four twisted turns in the coupling region (twisted region). Diameter of the PTT nanowires used is 440 nm and coupling region (inset of Figure 35d) is about 23 μm long and 880 nm wide. Both the input and the output branching angles, α and β are 20°.

For sensing applications, the twisted region (used as the sensing area) was immersed in various sample solutions with differing refractive indices. Then the output optical signals delivered through tapered fibers get detected by optical detector and fed to power meter. In our characterization, sodium chloride aqueous solutions with different mass concentrations (different refractive indices of surrounding mediums) were chosen as sample solutions. Each solution droplet was dropped on the sensing area of the sensor using a micro-injector. After each measurement, the sensor was cleaned by purified water and dried for different concentration solution use.
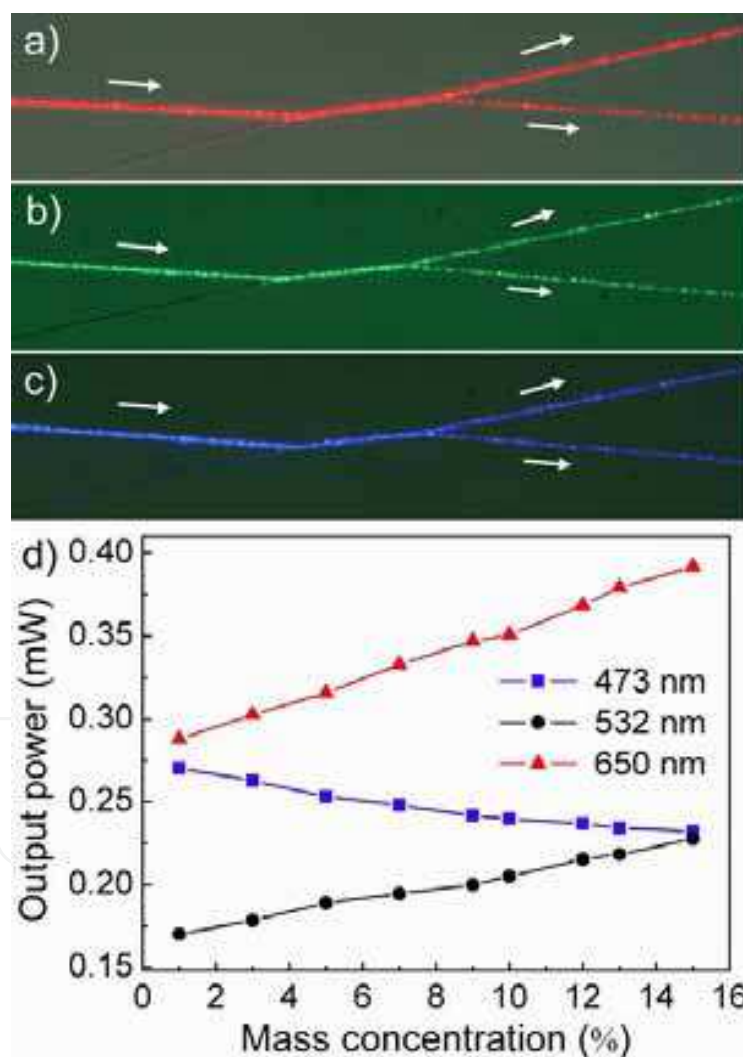

Fig. 36. Optical microscope images of the sensor with (a) red light (λ = 650 nm), (b) green light (λ = 532 nm), and (c) blue light (λ = 473 nm) in it (without sample solution). The white arrows show the propagation directions of the light. (d) Output power in the output branch 1 as a function of mass concentration of solution at branching angles of 20° and light of different wavelengths (473, 532, and 650 nm).

Figure 36a–c show optical microscope images of red, green, and blue lights propagated in the sensor (without sample solution), respectively. The three wavelengths were launched individually. The output power splitting ratios are 70:30, 50:50, and 55:45, for red, green, and blue lights, respectively. Figure 36d shows the measured power (P_1) in the output branch 1 as a function of the mass concentration of the solution at branching angle of 20° for wavelengths of 473 nm, 532 nm, and 650 nm. As evident, the output power is approximately linearly related to the mass concentration. Therefore, there is a direct relationship between output power and refractive index. In reverse, one can get to know the matter of surrounding according to the changes of the output power. The sensitivity S of the sensor is defined as $S = |\Delta P_1/\Delta n|$, where ΔP_1 is the change of the output power in the output branch 1 and Δn is the change of the refractive index of surrounding medium. From Figure 36d, we have calculated that the sensitivities for the blue (473 nm), green (532 nm), and red (650 nm) lights are 1.47, 2.19, and 4.25 mW/RIU (refractive index unit), respectively. Since the resolution of the optical power meter, which we have used is 5 nW, therefore, the detection limits on the refractive index change are about 3.40×10^{-6} (blue light), 2.28×10^{-6} (green light), and 1.18×10^{-6} (red light) for the sensor with four twisted turns in the sensing area.

The sensing mechanism of the twisted 2×2 coupling sensor can be explained as follows: Since the structure was assembled by the nanometer-scale PTT wires, launched light will be guided along the nanowires as strong evanescent waves. The change of the refractive index in the surrounding medium results in the change of the mode profile. As a result, the optical coupling property between the two nanowires in the sensing area (twisted region or coupling region) will be different and the optical power in the output branches will be changed.

To investigate influence of twisted turns on the sensing properties of the 2×2 coupling sensor, the number of the twisted turns was changed by rotating the right support. Figure 37a shows the measured output power change in the output branch 1 as a function of the refractive index at different twisted turns (2, 3, 4, 6, 8, 12, 16, 20, 23 and 24 turns). The change of the angles α and β caused by the change of the twisted turns was ignored here. In experiment, a longer coupling region causes a larger output power change for the same refractive index change. As a result, the sensitivity increases with the increase of the twisted turns. The sensitivity will reaches a maximum value when the twisted turns reach a particular value. In case of continuous increase in the twisted turns, the output power in the output branch will no longer be a monotone function of the refractive index and will not be able to decide the refractive index of the surrounding medium according to the output power. In experiment, the refractive index varies from 1.3321 to 1.3565 for red light, the sensitivity reaches a maximum when the twisted turns is 23. Figure 37b shows the sensitivity versus the twisted turns. The calculated highest sensitivity is about 26.96 mW/RIU. In this scenario, the calculated detection limit on the refractive index change is about 1.85×10^{-7} and the measured tenability is 1.2 mW per RIU per twisted turn.

To investigate tunability and/or branching angle dependence of the sensor, each branch end of the 2×2 sensor was removed from the microstage supports and refixed by the PTT melt on four tunable microstage supports as shown schematically in Figure 38. Since the sensitivity of the sensor increases with the twisted turns and reaches a maximum value at 23 twisted turns, we chose a twisted turn number less than 23 to investigate the branching angle dependence. As an example, we rotated the sensor to 14 twisted turns and fixed it on the tunable microstage supports as shown in Figure 38. It should be pointed out that the branching angles of the sensor are changeable by adjusting the tunable microstage supports.
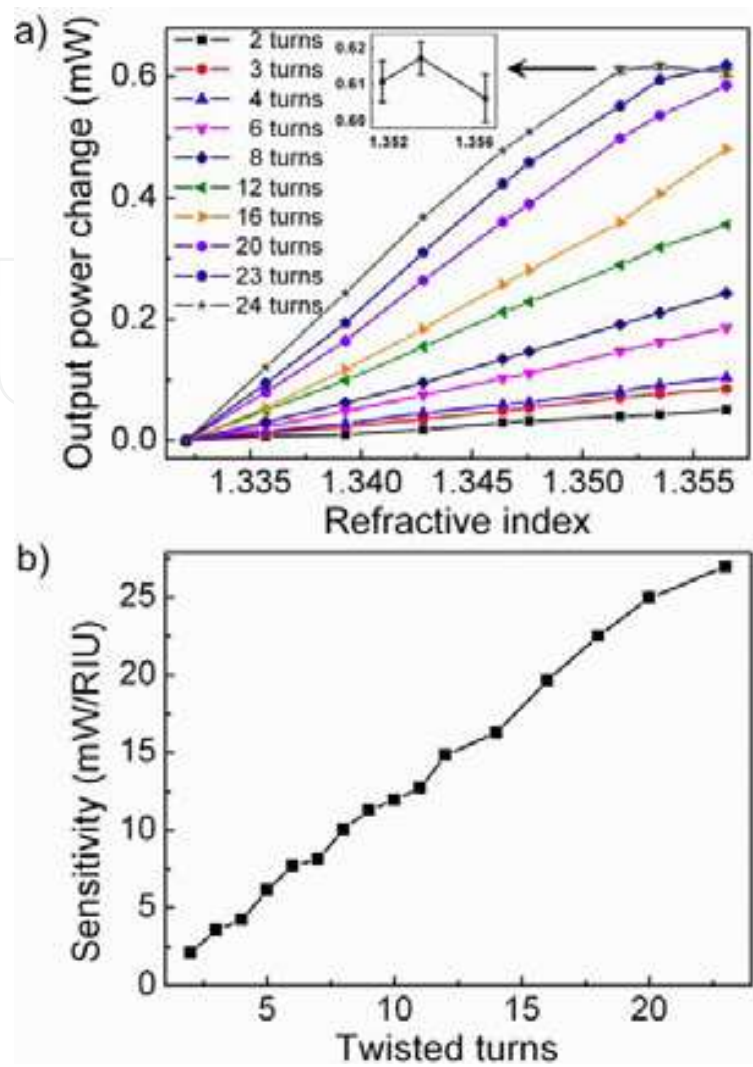
Fig. 37. Twisted turn dependence of the sensor. (a) Output power change in the output branch 1 as a function of refractive index at 650 nm wavelength with different twisted turns. The diameter of the nanowire is 440 nm and the input/output branching angles are around 20°. The inset shows error bars of the output power for 24 turns with refractive index larger than 1.35. (b) The sensitivity of the sensor *versus* the twisted turns.
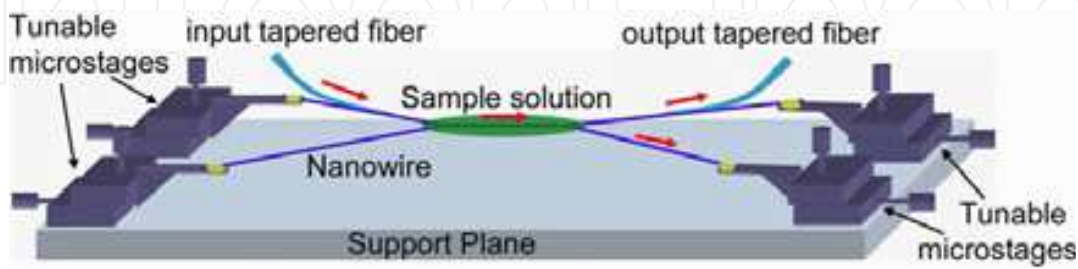

Fig. 38. Schematic diagram of the sensor with 14 twisted turns for tunable characterization. Each end of the sensor was fixed by a tunable microstage. The sensing area was immersed into different sample solutions. Red arrows show the propagation directions of the light. The light is launched into the sensor by the input tapered fiber and collected by the output tapered fiber.

The input/output branching angles α and β were changed from 5º to 35º with a step of 5º by moving the tunable microstages. Figure 39a shows the measured output power change in the output branch 1 with different branching angles at 650 nm wavelength. The measured tunability is 1.8 mW per RIU per 5° branching angle change. Experimental results show that the sensitivity becomes higher with smaller angles of α and β, which is shown in Figure 39b. This can be explained as that the effective coupling length decreases when the branching angle increases, which results in a decrease of the sensitivity. Another reason is that the bending loss in the branching region increase when the branching angle increases, leading to a decrease of the change amplitude of the output power for the same refractive index change, which will lower sensitivity.
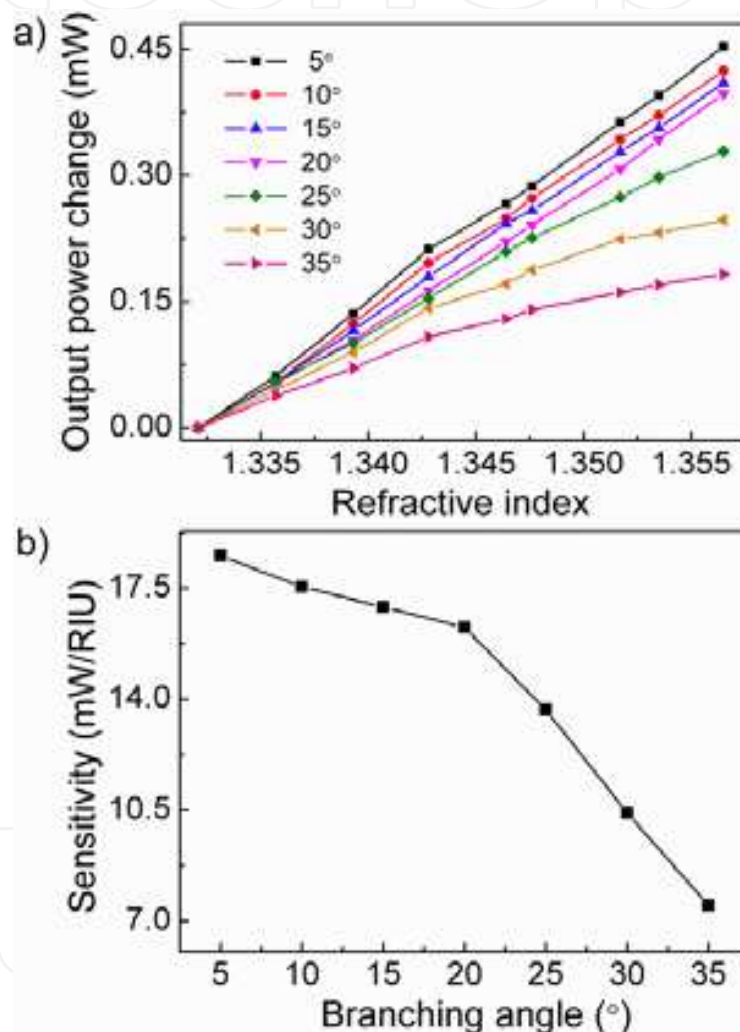

Fig. 39. Input/output branching angle dependence of the sensor. (a) Output power change in the output branch 1 as a function of refractive index at 650 nm red light with different branching angles and 14 twisted turns. Input/output branching angles change from 5º to 35º with a step of 5º. (b) The sensitivity of the sensor *versus* the branching angles.

The highest sensitivity of sensor is 26.96 mW/RIU with 23 twisted turns at 650 nm red light and the refractive index detection limit is 1.85×10^{-7}, while the sensing area is about 130 μm long and 880 nm wide. The properties of the sensor can be tuned by changing the input/output branching angles or the twisted turns. The average tunability are 1.2 mW per

RIU per twisted turn and 1.8 mW per RIU per 5° branching angle change. The ultracompact, highly sensitive and tunable refractive index sensor would be useful in physics, biology, biochemistry, environmental, and toxicant sensing, while the easy, cheap, and fast twist technology would be promising in fabricating of multiterminal nanosensors.

7. Perspectives

PTT nanowires can be easily drawn by the one-step direct drawing technique and with very well surface smoothness, length uniformity, and mechanical strength. PTT nanowire-based devices including optical beam splitters, couplers, nanorings, tweezer/scissor-shaped structures, and a series of nanophotonic device arrays have been assembled. Their application in sensor has also been demonstrated. Apply elastic PTT nanowires to nanodiaply would be an interesting topic in the future. In addition, by adopting photosensitive materials such as rare-earth into the PTT melt, more versatile nanowires could be obtained and more promising nanophotonic devices could be realized.

8. References

[1] D. Appell, "Wired for success," Nature 419, 553-555 (2002).

[2] M. Law, D. J. Sirbuly, J. C. Johnson, J. Goldberger, R. J. Saykally, and P. Yang, "Nanoribbon waveguides for subwavelength photonics integration," Science 305, 1269-1273 (2004).

[3] L. Tong, R. R. Gattass, J. B. Ashcom, S. He, J. Lou, M. Shen, I. Maxwell, and E. Mazur, "Subwavelength-diameter silica wires for low-loss optical wave guiding," Nature 426, 816-819 (2003).

[4] L. Tong, L. Hu, J. Zhang, J. Qiu, Q. Yang, J. Lou, Y. Shen, J. He, and Z. Ye, "Photonic nanowires directly drawn from bulk glasses," Opt. Express 14, 82-87 (2006).

[5] J. C. Knight, G. Cheung, F. Jacques, and T. A. Birks, "Phase-matched excitation of whispering-gallery-mode resonances by a fiber taper," Opt. Lett. 22, 1129-1131 (1997).

[6] G. Brambilla, V. Finazzi, and D. J. Richardson, "Ultra-low-loss optical fiber nanotapers," Opt. Express 12, 2258-2263 (2004).

[7] G. Brambilla, F. Xu, and X. Feng, "Fabrication of optical fiber nanowires and their optical and mechanical characterisation," Electron. Lett. 42, 517-518 (2006).

[8] G. Brambilla, F. Koizumi, X. Feng, and D. J. Richardson, "Compound-glass optical nanowires," Electron. Lett. 41, 400-401 (2005).

[9] L. Tong, J. Lou, R. R. Gattass, S. He, X. Chen, L. Liu, and E. Mazur, "Assembly of silica nanowires on silica aerogels for microphotonic devices," Nano Lett. 5, 259-262 (2005).

[10] Y. Li and L. Tong, "Mach-Zehnder interferometers assembled with optical microfibers or nanofibers," Opt. Lett. 33, 303-305 (2008).

[11] S. A. Harfenist, S. D. Cambron, E. W. Nelson, S. M. Berry, A. W. Isham, M. M. Crain, K. M. Walsh, R. S. Keynton, and R. W. Cohn, "Direct drawing of suspended filamentary micro- and nanostructures from liquid polymers," Nano Lett. 4, 1931-1937 (2004).

[12] H. Liu, J. B. Edel, L. M. Bellan, and H. G. Craighead, "Electrospun polymer nanofibers as subwavelength optical waveguides incorporating quantum dots," Small 2, 495-499 (2006).

[13] J. R. Whinfield and J. T. Dickson, British Patent, 578, 079 (1946).

[14] H. H. Chuah, "Crystallization kinetics of poIy(trimethyIene terephthalate)," Polym. Eng. Sci. 41, 308-313 (2001).

[15] I. M. Ward, M. A. Wilding, and H. Brody, "The mechanical properties and structure of poly(m-methylene terephthalate) fibers," J. Polym. Sci., Polym. Phys. Ed. 14, 263-274 (1976).

[16] Process Economics Prcgrarn Report 227. 1.3-propanedwl and polytrimethylene terephthalate, SRI International (1999).

[17] J. S. Grebowicz and H. H. Chuah, "Thermal properties of poly(propylene terephthalate)," Research Awareness Bulletin, Shell Chemical Company, Houston, TX, 97-100 (1993).

[18] M. Pyda, A. Boller, J. Grebowicz, H. Chuah, B. V. Lebedev, and B. Wunderlich, "Heat capacity of poly(trimethylene terephthalate)," J. Polym. Sci., Polym. Phys. Ed. 36, 2499-2511 (1998).

[19] K. M. Lee, K. J. Kim, and Y. H. Kim, "Isothermal crystallization behavior and some physical parameters of poly(trimethylene terephthalate)," Polymer (Korea) 23, 56-65 (1999).

[20] J. M. Huang and F. C. Chang, "Crystallization kinetics of poly(trimethylene terephthalate)," J. Polym. Sci., Polym. Phys. Ed. 38, 934-941 (2000).

[21] J. M. Huang, M. Y. Ju, P. P. Chu, and F. C. Chang, "Crystallization and melting behaviors of poly(trimethylene terephthalate)," J. Polym. Res. 6, 259-266 (1999).

[22] K. Dangayach, H. Chuah, W. Gergen, P. Dalton, and F. Smith, "Poly(trimethylene terephthalate) – a new opportunity in engineering thermoplastic applications," Proceedings of the 55th SPE ANTEC'97 Conference, June 16–20, 1997, Chicago, IL, Society of Plastics Engineers, Brookfield, CT, 2097-2101 (1997).

[23] K. Dangayach, K. Ghosh, H. H. Chuah, B. Cristea, and W. P. Gergen, "PTT – a new polymer for engineering applications," ETP'99 Conference, June 7–9, 1999, Zurich, Switzerland, Maack Conference (1999).

[24] H. H. Chuah, "Intrinsic birefringence of poly(trimethylene terephthalate)," J. Polym. Sci.: Part B: Polym. Phys. 40, 1513-1520 (2002).

[25] X. B. Xing, H. Zhu, Y. Q. Wang, and B. J. Li, "Ultracompact photonic coupling splitters twisted by PTT nanowires," Nano Lett. 8, 2839-2843 (2008).

[26] J. Scheirs and T. E. Long, Modern polyesters: chemistry and technology of polyesters and copolyesters, John Wiley & Sons, 2003.

[27] R. Jakeways, I. M. Ward, M. A. Wilding, I. J. Desborough, and M. G. Pass, "Crystal deformation in aromatic polyesters," J. Polym. Sci., Polym. Phys. Ed. 13, 799-813 (1975).

[28] U. W. Gedde, Polymer Physics, Chapman & Hall, London, 1995.

[29] K. Nakamae, T. Nishio, K. Hata, F. Yokoyama, and T. Matsumoto, "Elastic moduli of the crystalline region of polytrimethylene terephthalate," J. Soc. Mater. Sci , Jpn., 35, 1066-1070 (1986).

[30] W. H. Jo, "Polymorphism and surface properties of poly(trimethylene terephthalate) (PTT)," Final Report, Shell Chemical Company, Houston, Tx, 1999.

[31] H. H. Chuah, "Orientation and structure development in poly(trimethylene terephthalate) tensile drawing," Macromolecules 34, 6985-6993 (2001).

[32] M. S. Khil, H. Y. Kim, M. S. Kim, S. Y. Park, and D.-R. Lee, "Nanofibrous mats of poly(trimethylene terephthalate) via electrospinning," Polymer 45, 295-301 (2004).

[33] W. He, B. J. Li, and E. Y.-B. Pun, "Wavelength, cross-angle, and core-diameter dependence of coupling efficiency in nanowire evanescent wave coupling," Opt. Lett. 34, 1597-1599 (2009).

[34] X. B. Xing, Y. Q. Wang, and B. J. Li, "Nanofiber drawing and nanodevice assembly in poly(trimethylene terephthalate)," Opt. Express 16, 10815-10822 (2008).

[35] X. B. Xing, H. Zhu, Y. Q. Wang, and B. J. Li, "Ultracompact photonic coupling splitters twisted by PTT nanowires," Nano Lett. 8, 2839-2843 (2008).

[36] Y. Q. Wang, H. Zhu, and B. J. Li, "Cascaded Mach-Zehnder interferometers assembled by submicrometer PTT wires," IEEE Photon. Technol. Lett. 21, 1115-1117 (2009).

[37] H. Zhu, Y. Q. Wang, and B. J. Li, "Tunable refractive index sensor with ultracompact structure twisted by poly(trimethylene terephthalate) nanowires," ACS Nano 3, 3110-3114 (2009).

Nanowires Science and Technology

Edited by Nicoleta Lupu

This book describes nanowires fabrication and their potential applications, both as standing alone or complementing carbon nanotubes and polymers. Understanding the design and working principles of nanowires described here, requires a multidisciplinary background of physics, chemistry, materials science, electrical and optoelectronics engineering, bioengineering, etc. This book is organized in eighteen chapters. In the first chapters, some considerations concerning the preparation of metallic and semiconductor nanowires are presented. Then, combinations of nanowires and carbon nanotubes are described and their properties connected with possible applications. After that, some polymer nanowires single or complementing metallic nanowires are reported. A new family of nanowires, the photoferroelectric ones, is presented in connection with their possible applications in non-volatile memory devices. Finally, some applications of nanowires in Magnetic Resonance Imaging, photoluminescence, light sensing and field-effect transistors are described. The book offers new insights, solutions and ideas for the design of efficient nanowires and applications. While not pretending to be comprehensive, its wide coverage might be appropriate not only for researchers but also for experienced technical professionals.

INTECH
open science | open minds